

FACULTY
OF MATHEMATICS
AND PHYSICS
Charles University

1

BACHELOR THESIS

2

Martin Vavřík

3

**Simulation and Reconstruction
of Charged Particle Trajectories
in an Atypic Time Projection Chamber**

4

5

Institute of Particle and Nuclear Physics

6

Supervisor of the bachelor thesis: Mgr. Tomáš Sýkora, Ph.D.

7

Study programme: Physics

8

Prague 2025

- ⁹ I declare that I carried out this bachelor thesis independently, and only with the
¹⁰ cited sources, literature and other professional sources. It has not been used to
¹¹ obtain another or the same degree.
- ¹² I understand that my work relates to the rights and obligations under the Act
¹³ No. 121/2000 Sb., the Copyright Act, as amended, in particular the fact that the
¹⁴ Charles University has the right to conclude a license agreement on the use of this
¹⁵ work as a school work pursuant to Section 60 subsection 1 of the Copyright Act.

In date
Author's signature

¹⁶ Dedication.

Title: Simulation and Reconstruction of Charged Particle Trajectories in an Atypical Time Projection Chamber **Added hyphen to avoid overfull hbox**

Author: Martin Vavřík

Institute: Institute of Particle and Nuclear Physics

Supervisor: Mgr. Tomáš Sýkora, Ph.D., Institute of Particle and Nuclear Physics

Abstract: Abstract.

Keywords: key words

¹⁷ Contents

¹⁸	Motivation	³
¹⁹	0.1 ATOMKI Anomaly	³
²⁰	0.1.1 ATOMKI Measurements	³
²¹	0.1.2 Other Experiments	⁴
²²	0.2 X17 Project at IEAP CTU	⁶
²³	1 Time Projection Chamber	⁹
²⁴	1.1 Charge transport in gases	¹⁰
²⁵	1.1.1 Drift	¹⁰
²⁶	1.1.2 Diffusion	¹¹
²⁷	1.2 Readout	¹²
²⁸	1.2.1 Multi-Wire Proportional Chamber	¹²
²⁹	1.2.2 Gas Electron Multiplier	¹²
³⁰	1.2.3 Micromegas	¹²
³¹	1.2.4 Parallel Plate Chamber	¹⁴
³²	1.3 Orthogonal Fields TPC at IEAP CTU	¹⁴
³³	1.3.1 Motivation and Associated Challenges	¹⁴
³⁴	1.3.2 Coordinate Systems and Dimensions	¹⁴
³⁵	1.3.3 Magnetic Field Simulation	¹⁷
³⁶	2 Track Simulation	²⁰
³⁷	2.1 Microscopic Simulation	²⁰
³⁸	2.1.1 First testing track	²¹
³⁹	2.1.2 Grid-like testing sample	²¹
⁴⁰	2.2 Runge-Kutta Simulation	²¹
⁴¹	2.2.1 Testing sample	²⁴
⁴²	3 Track Reconstruction	²⁶
⁴³	3.1 Reconstruction Assuming Steady Drift	²⁶
⁴⁴	3.2 Ionization Electron Map	²⁷
⁴⁵	3.2.1 Gradient Descent Algorithm	³⁴
⁴⁶	3.2.2 Interpolation on the Inverse Grid	³⁵
⁴⁷	3.3 Discrete Reconstruction	³⁷
⁴⁸	4 Energy Reconstruction	³⁹
⁴⁹	4.1 Cubic Spline Fit	³⁹
⁵⁰	4.2 Circle and Lines Fit	⁴¹
⁵¹	4.2.1 Two-dimensional fit	⁴²
⁵²	4.2.2 Three-dimensional fit	⁴³
⁵³	4.2.3 Testing on a Runge-Kutta sample	⁴⁵
⁵⁴	4.3 Runge-Kutta Fit	⁴⁶
⁵⁵	4.3.1 Testing on a microscopic sample	⁴⁸
⁵⁶	Conclusion	⁵⁰
⁵⁷	Bibliography	⁵⁴

⁵⁹ Motivation

⁶⁰ A Time Projection Chamber (TPC) [refs] is a type of gaseous detector that detects
⁶¹ charged particle trajectories by measuring the positions and drift time of ions cre-
⁶² ated in the gas. The energies of these particles can be inferred from the curvatures
⁶³ of their trajectories in the magnetic field (specific field inside the TPC).

⁶⁴ The goal of this thesis is to develop an algorithm for the reconstruction of
⁶⁵ charged particle trajectories and energy in an *atypic* TPC with orthogonal elec-
⁶⁶ tric and magnetic fields, hereafter referred to as the Orthogonal Fields TPC
⁶⁷ (OFTPC), used in the X17 project at the Institute of Experimental and Ap-
⁶⁸ plied Physics, Czech Technical University in Prague (IEAP CTU). Furthermore,
⁶⁹ we present the results of testing of several (gradually improving) developed algo-
⁷⁰ rithms with different samples of simulated data. Put this somewhere, (maybe just
⁷¹ the abstract?). We use the Garfield++ toolkit [1] for simulations in combination
⁷² with the ROOT framework [2] for data analysis and visualization. Some of our
⁷³ more demanding simulations are run on the MetaCentrum grid [3].

⁷⁴ The X17 project in IEAP CTU aims to reproduce measurements of anomalous
⁷⁵ behavior in the angular correlation distribution of pairs produced by the Internal
⁷⁶ Pair Creation (IPC) mechanism [4] during the decay of certain excited nuclei
⁷⁷ (⁸Be, ¹²C, and ⁴He) observed by a team at ATOMKI in Hungary. I would leave
⁷⁸ this here as a short summary before I explain it in more detail in the sections
⁷⁹ below.

⁸⁰ Add citations: X17 project, VdG. Maybe also TPC, etc.

⁸¹ 0.1 ATOMKI Anomaly

⁸² Many different theories propose the existence of *new light boson(s)* that are weakly
⁸³ coupled to ordinary matter [5]. These particles are potential dark matter candi-
⁸⁴ dates and could contribute to a solution of other issues with the Standard Model,
⁸⁵ such as the strong CP problem and the anomalous muon magnetic moment. Mass
⁸⁶ range of axions?

⁸⁷ A possible way of detecting such bosons with a short lifetime is to observe
⁸⁸ nuclear transitions of excited nuclei. If a boson was emitted during the transition
⁸⁹ and subsequently decayed into an electron-positron pair, we could observe this as
⁹⁰ a peak on top of the standard e^+e^- (both cursive and upright forms are used in
⁹¹ different articles) angular correlation from the Internal Pair Creation (IPC) and
⁹² the External Pair Creation (EPC).

⁹³ 0.1.1 ATOMKI Measurements

⁹⁴ Historically, there were several measurements of the IPC in nuclear transitions
⁹⁵ in ⁸Be at Institute für Kernphysik (Frankfurt) [6, 7, 8] and at ATOMKI (De-
⁹⁶ brecen, Hungary) [9, 10] resulting in different anomalies with invariant mass in
⁹⁷ the range 5 – 15 MeV. This prompted a development of a better spectrometer at
⁹⁸ ATOMKI.

⁹⁹ In 2015, a group at ATOMKI observed an anomalous IPC in ⁸Be [11]. They
¹⁰⁰ used the ${}^7\text{Li}(p, \gamma){}^8\text{Be}$ reaction at the $E_p = 1030$ keV proton capture resonance

to prepare the 18.15 MeV excited state ($J^\pi = 1^+$, $T = 0$). This state decays predominantly through M1 transitions to the ground state ($J^\pi = 0^+$, $T = 0$) and to the 3.03 MeV state ($J^\pi = 2^+$, $T = 0$) [12]. **Transition figure – all transitions of isotopes? IPC figure?**

The angular correlation of the e^+e^- pairs created internally in these transitions were measured and compared to the simulation; results from a narrow $E_{\text{sum}} = 18$ MeV region are shown in Figure 0.1a. The simulation includes boson decay pairs for different boson masses. The disparity parameter y is defined as

$$y = \frac{E_{e^-} - E_{e^+}}{E_{e^-} + E_{e^+}}, \quad (0.1)$$

where E_{e^-} and E_{e^+} are the kinetic energies of the electron and positron.

Their experimental setup was later upgraded (**details?**) and used for new measurements. In 2022 the ${}^8\text{Be}$ anomaly was also measured using the $E_p = 441$ keV resonance to produce the 17.64 MeV excited state ($J^\pi = 1^+$, $T = 1$) which again decays primarily to the ground state and the 3.03 MeV state [12]. The anomaly was also measured for $E_p = 650$ and 800 keV where E1 transitions from the direct proton capture dominate [13]. The results for e^+e^- with $E_{\text{sum}} \in [13.5, 20]$ MeV are shown in Figure 0.1b.

The newer setup was also used in 2021 to study the ${}^3\text{H}(p, e^+e^-){}^4\text{He}$ reaction at $E_p = 510, 610$ and 900 keV [14], inducing direct and resonant capture populating the overlapping first 20.21 MeV ($J^\pi = 0^+$) and second 21.01 MeV ($J^\pi = 0^-$) excited states [15]. The comparison of simulated and measured e^+e^- pair angular correlations in the $E_{\text{sum}} \in [18, 22]$ MeV region is shown in Figure 0.1c.

In 2022, another anomaly was measured in the ${}^{11}\text{B}(p, e^+e^-){}^{12}\text{C}$ process [16]. The $E_p = 1388$ keV resonance was used to populate the 17.23 MeV excited state ($J^\pi = 1^-$, $T = 1$) with a large width $\Gamma = 1.15$ MeV [17]. This state decays mainly through E1 transitions to the ground state $J^\pi = 0^+$ and to the 4.44 MeV state $J^\pi = 2^+$. To compensate for energy losses in the target, five energies in the range $E_p = 1.5\text{--}2.5$ MeV were used. The experimental angular correlation for the 17.23 MeV transition to the ground state is shown in Figure 0.1d.

Possible explanations of the anomaly include experimental effects, higher order processes in the Standard Model [18, 19] or even a protophobic fifth force mediated by a new 17 MeV boson X17 [20]. **Not sure if the introduction should be referenced since even though it is related, it is an independent theory developed only (?) to explain these measurements. Zhang and Miller: <https://www.sciencedirect.com/science/article/pii/S0370269321000010>**

0.1.2 Other Experiments

Since the ATOMKI measurements, several experiments have been initiated to attempt to replicate the results and search for the hypothetical X17 particle. The following experiments have already produced results. **Could cite the ATOMKI review paper here.**

Two-arm e^+e^- spectrometer in Hanoi

The anomaly in ${}^8\text{Be}$ has been observed with a high ($> 4\sigma$ **That's all they write in their article.**) confidence by a team at the Hanoi University of Sciences for

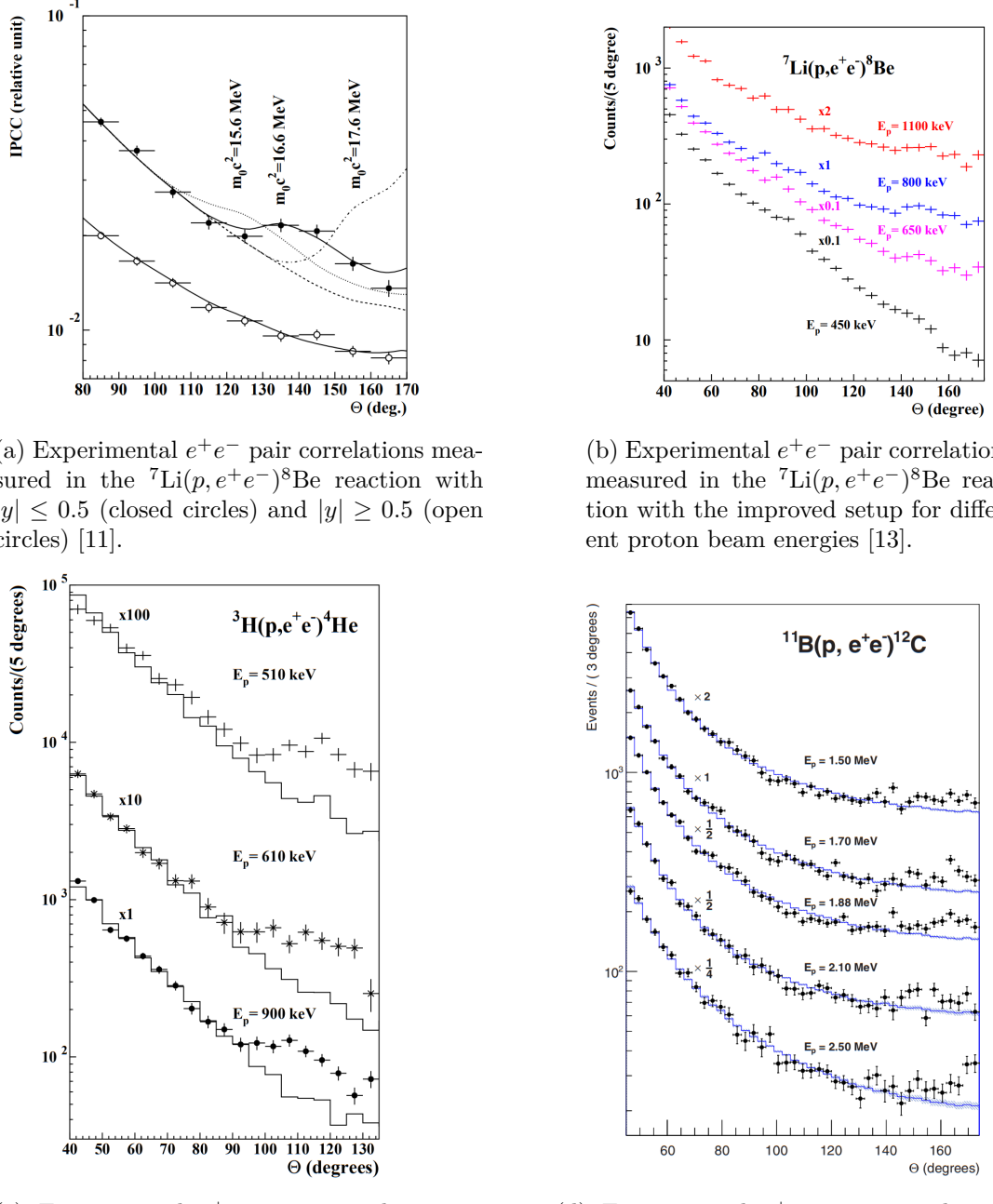


Figure 0.1: The ATOMKI anomalous IPC measured for different nuclei.



Figure 0.2: Results from the Hanoi spectrometer – angular e^+e^- pair correlations measured in the ${}^7\text{Li}(p, e^+e^-){}^8\text{Be}$ reaction at $E_p = 1225$ keV [21].

143 $E_p = 1225$ keV [21]. They built a two-arm spectrometer in collaboration with
144 ATOMKI and calibrated it using the 17.6 MeV M1 transition. The results are
145 shown in Figure 0.2.

146 Collisions at Nuclotron in Dubna

147 At the Joint Institute for Nuclear Research in Dubna, signal in the form of en-
148 hanced structures in the $\gamma\gamma$ spectra at ~ 17 and 38 MeV invariant masses for
149 $p + \text{C}$, $d + \text{C}$ and $d + \text{Cu}$ reactions at momenta 5.5 , 2.75 , and 3.83 GeV per nu-
150 cleon [22]. Monte Carlo simulations support the conclusion that the signals are
151 a consequence of a decay of unknown particles X17 and E38.

152 The MEG II (Muon Electron Gamma) experiment

153 Experiments using the ${}^7\text{Li}(p, e^+e^-){}^8\text{Be}$ reaction were carried out at the Paul
154 Scherrer Institute with the MEG II superconducting solenoid spectrometer [23].
155 Analysis of the data with $E_p = 1080$ keV exciting both of the resonances (beam
156 fully stopping in the target) found no significant evidence supporting the X17
157 hypothesis, results are shown in Figure 0.3. An upper bound (at 90% confidence)
158 on the X17-to- γ branching ratio was set at $1.2 \cdot 10^{-5}$ for the 18.15 MeV state
159 (larger than the ratio $5.8 \cdot 10^{-6}$ obtained by ATOMKI in 2016). Could add their
160 90% C.L bounds figure also. Insufficient statistics – 6.2 % (1.5σ) p-value.

161 0.2 X17 Project at IEAP CTU

162 The aim of the X17 project at the Van der Graaff facility of the Institute of Experi-
163 mental and Applied Physics, Czech Technical University in Prague is to repeat the
164 original ATOMKI experiments with ${}^7\text{Li}$ and ${}^3\text{H}$ targets using an independent e^+e^-
165 spectrometer. In order to effectively measure the anomaly, we need to reconstruct

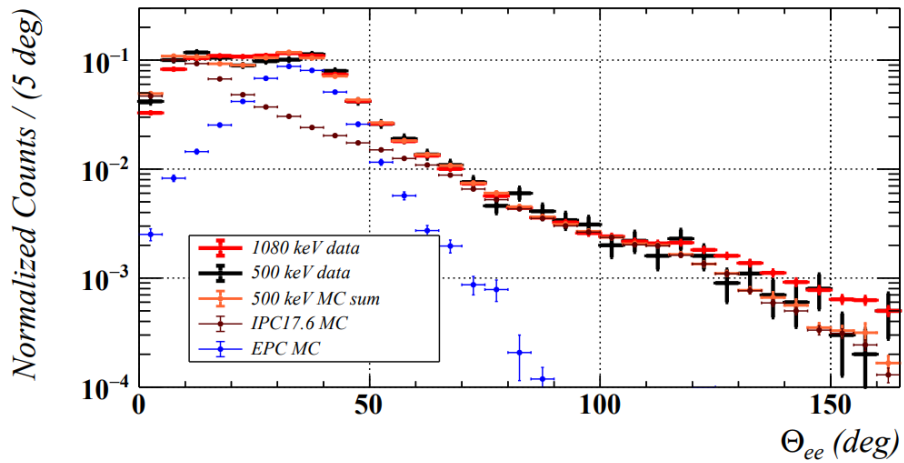


Figure 0.3: Results from the MEG II experiments – angular correlation of e^+e^- pairs with $E_{\text{sum}} \in [16, 20]$ MeV measured in the ${}^7\text{Li}(p, e^+e^-){}^8\text{Be}$ reaction with proton beam energies 500 and 1080 keV. The 500 keV dataset is fitted with Monte Carlo of both the IPC deexcitation and the EPC produced by gammas [23].

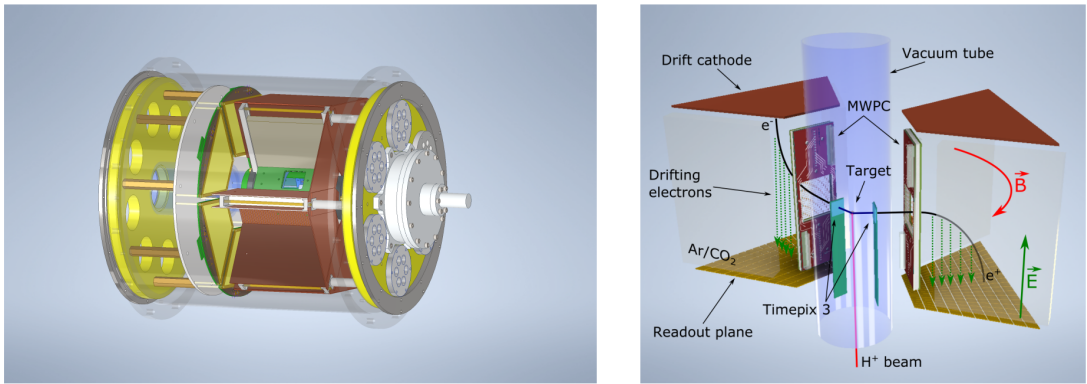


Figure 0.4: Schematics of the detector at the Van der Graaff facility at IEAP CTU.

166 both the energy and the angular correlation of the e^+e^- pairs. The spectrometer
 167 will use three layers of detectors to achieve this – Timepix 3 (TPX3) silicon
 168 pixel detector and Multi-Wire Proportional Chamber (MWPC) layers for the an-
 169 gle reconstruction and a Time Projection Chamber (TPC) layer for the energy
 170 reconstruction. The schematics of the prepared detector is in Figure 0.4 Spec-
 171 trometer CAD drawing (coordinates here or next chapter?). Cite some VdG
 172 paper, mention grant? Using [https://cernbox.cern.ch/pdf-viewer/public/
 173 rf0oU1nqVLN3acZ/LuzH_submitted.pdf](https://cernbox.cern.ch/pdf-viewer/public/rf0oU1nqVLN3acZ/LuzH_submitted.pdf).

174 The energy of e^+e^- pair produced in the reaction is given by the energy
 175 available E_r in the reaction and can be distributed between them arbitrarily.
 176 Nonetheless in the decay of the hypothetical X17 particle, electron and positron
 177 should have similar energy and we can therefore use a disparity cut $|y| \leq 0.5$
 178 for the disparity parameter (defined in Equation 0.1). Interesting events should
 179 rarely have a particle with an energy below $E_r/4$ (roughly 4 MeV). Electrons with
 180 such low energies are scattered significantly by even a thin layer of relatively light

181 material, for this reason the TPX3 layer will be inside of the vacuum tube and
182 the tube will have a thinned aluminum segment or Kapton™ windows.

183 TPX3 can measure (in each $55 \times 55 \mu\text{m}$ pixel of its 256×256 grid) time-of-arrival |
184 (ToA) with 1.6 ns precision and time-over-threshold (ToT) which reflects the de-
185 posited energy. This potentially allows 3D tracking if we increase the chip thick-
186 ness at the cost of increased scattering. The layer can reconstruct the reaction
187 vertex and the angular correlation with high precision.

188 The layer of MWPCs with sensitive area $40 \times 38 \text{ mm}^2$ will be outside of
189 the beam pipe. It will provide an extra point on the particle trajectory which can
190 help with the estimation of the reaction vertex and improve the TPC performance
191 by providing its entry point.

192 The TPCs, which are a subject of this theses, are in a magnetic field of per-
193 manent magnets positioned between them and provide 3D track reconstruction
194 and subsequent momentum and particle identification (its charge, or even type
195 based on its stopping power). They avoid radiative losses thanks to the small
196 interaction with the incident particle. For the readout, triple Gas Electron Mul-
197 tiplier (GEM) will be used. The magnetic field layout in our TPCs is atypical –
198 orthogonal to the electric field inside the chamber, this is why we call them Or-
199 thogonal Fields TPC (OFTPC). Further details about our OFTPCs are provided
200 in section 1.3.

1. Time Projection Chamber

201 202 Using (2010 – a little old) <https://cds.cern.ch/record/1302071/files/CERN-PH-EP-2010-047.pdf>
203 204 A Time Projection Chamber (TPC) is a type of gaseous detector that uses
205 206 the drift in an electric field of free charges (electrons and cations, also anions if
207 208 attachment of electrons to the gas particles is considered) produced by an ionizing
209 210 particle to reconstruct its 3D trajectory. When placed inside a magnetic field,
the momentum of the incident particle can be inferred from the curvature of its
trajectory. Particle identification is also possible using the ionization energy loss
inside the TPC (see Figure 1.1). The detector used 80:20 Ar:CH₄ mixture at
8.5 atm pressure.

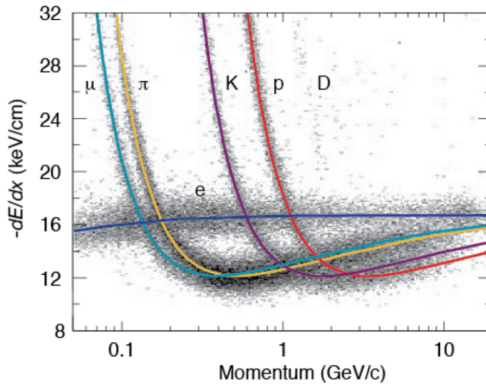


Figure 1.1: Particle identification in the PEP-4 TPC at SLAC based on the energy loss per distance $\frac{dE}{dx}$ [24].

211 The original TPC used in the PEP-4 experiment at SLAC (Figure 1.2) was
212 213 a 2×2 m cylinder with a central cathode that produced a strong electric field,
making the ionization electrons drift towards one of the bases. The readout
214 215 consisted of MWPCs, where electrons are accelerated towards the anode wires
enough to further ionize the gas and cause an avalanche.

216 When a charged particle crosses the volume of a TPC, it loses energy by exci-
217 218 tation and ionization of the detector gas (how much – from $dE/dx +$ density \rightarrow
footnote?). Most ionizing collision produce a single ionization electron, sometimes
219 220 a few secondary electrons are produced close to the collision vertex. In rare cases,
221 222 the ionization electron has energy large enough to create a measurable track, such
223 224 an electron is called a δ -electron (terminology, just like below – technically it's
a (primary) ionization electron causing other (secondary) ionization). Penning
transfer (collisions, light – factor 10 for gas gain in Ar/CO₂ viz PDG CERN)?

225 CERES/NA45 – very inhomogeneous magnetic field. They used look-up ta-
226 227 bles for reconstruction, which they calculated by integrating the Langevin drift
velocity equation with Runge-Kutta.

228 From [26]:

229 230 10.2 Coordinate transformation The detector specific hit coordinates (pad, time,
plane) are transformed to spatial coordinates (x, y, z) via look-up tables. The
231 232 transformation contains the information about the transport process of the charged
clusters in the electric and magnetic fields inside the TPC. The look-up tables
are calculated using a Runge-Kutta method [39] that calculates the drift trajec-

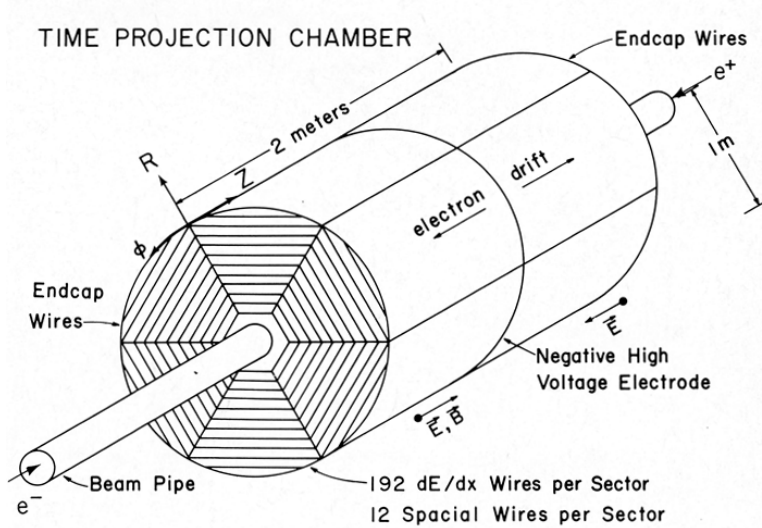


Figure 1.2: Schematic view of the PEP-4 TPC [25]. A charged particle produced in a collision in the beam pipe creates a spiral ionization track in the magnetic field. The central cathode then accelerates ionization electrons towards the endcap anode wires where they are multiplied and read out.

233 tory using in each point the drift velocity vector (Eq. 3), starting at the cathode
 234 plane. The drift between the cathode plane and the pad plane is absorbed in a
 235 φ -dependent time offset due the fact that each Front-End Electronic (FEE) chan-
 236 nel had a slightly different capacitance. The difference between the MAGBOLTZ
 237 Monte Carlo drift [19] and the actual drift velocity vector is accounted for with a
 238 z- and r(E)-dependent correction for the drift velocity component parallel to the
 239 electric field and the one parallel to $E \times B$

240 1.1 Charge transport in gases

241 1.1.1 Drift

242 Produced ionization electrons (terminology – called ionization electrons in the rest
 243 of the thesis, ionoelectrons?) are accelerated towards the readout by the electric
 244 field inside the chamber. At the same time, they lose speed by colliding with
 245 the gas particles, quickly reaching a constant (for a given field E, B) mean drift
 246 velocity. The electrons might be absorbed by electronegative impurities, such as
 247 halides and oxygen.

248 In many gases (called "hot", e.g., Ar or CH_4), the drift velocity (def? the
 249 paragraph above not enough?) is much greater than that of their thermal motion
 250 thanks to a high proportion of elastic collisions. On the other hand, "cold" gases
 251 like CO_2 have a higher proportion of inelastic collisions (e.g., thanks to the ex-
 252 citation of rotational and vibrational states) and therefore much lower (value?
 253 magnitude (implied)?) drift velocity.

254 The ions produced by the ionization lose a significant portion of their energy
 255 during each collision since their mass is close to the mass of the gas particles (see
 256 the source material – average energy loss during collision $\Delta E = \frac{2m_i M}{(m_i + M)^2}$, this way

257 it's more accurate). This, together with their large collision cross section, makes
 258 their drift velocity much smaller and their energy is close to thermal. Since their
 259 momenta aren't randomized to such an extent during collisions, their diffusion
 260 is smaller (more in the sense of distribution of positions, could move this to the
 261 diffusion subsection).

262 The drift is also influenced by the magnetic field. Langevin derived a good
 263 approximation for the drift velocity vector:

$$\mathbf{v}_d = \left(\frac{\mathbf{E}}{\|\mathbf{E}\|} + \omega\tau \frac{\mathbf{E} \times \mathbf{B}}{\|\mathbf{E}\| \|\mathbf{B}\|} + \omega^2\tau^2 \frac{\mathbf{E} \cdot \mathbf{B}}{\|\mathbf{E}\| \|\mathbf{B}\|} \cdot \frac{\mathbf{B}}{\|\mathbf{B}\|} \right) \frac{q\tau}{m(1 + \omega^2\tau^2)} \|\mathbf{E}\|, \quad (1.1)$$

264 where q is the charge of the particle, m is its mass, τ is the mean time between
 265 collisions and $\omega = \frac{q}{m} \|\mathbf{B}\|$ is the Larmor frequency. For orthogonal fields $\mathbf{E} \perp \mathbf{B}$,
 266 it can be shown that the magnetic field bends the direction of the drift by the
 267 so-called Lorentz angle:

$$\tan \psi = -\omega\tau. \quad (1.2)$$

268 The drift of ions is only negligibly influenced by the magnetic field ($\omega\tau \sim 10^{-4}$
 269 is small due to the low drift velocity – better (?) because it takes τ into account
 270 and differs only by E/B ratio (if the magnetic contribution to the magnitude
 271 is small)). In a standard TPC, \mathbf{E} is nearly parallel to \mathbf{B} and the influence of
 272 the magnetic field on the drift is minimal. Without magnetic field, we can write

$$\mathbf{v}_d = \frac{q\tau}{m} \mathbf{E} = \mu \mathbf{E}, \quad (1.3)$$

273 where μ is called charge mobility.

274 1.1.2 Diffusion

275 Due to collisions a cloud of electrons or ions originating from the same point will
 276 show a Gaussian density distribution at time t while drifting in the electric field
 277 $\mathbf{E} = (0, 0, E_z)$ along the z -coordinate (coordinates defined by the electric field):

$$\rho(x, y, z, t) = (4\pi Dt)^{-\frac{3}{2}} \exp\left(-\frac{x^2 + y^2 + (z - v_d t)^2}{4Dt}\right), \quad (1.4)$$

278 where the diffusion coefficient D can be expressed as

$$D = \frac{\lambda^2}{3\tau} = \frac{\lambda v_d}{3} = \frac{v_d^2 \tau}{3} = \frac{2\varepsilon\tau}{3m}, \quad (1.5)$$

279 where λ is the mean free path and ε the mean energy. The lateral diffusion width
 280 σ_x after a drift distance L can be expressed as

$$\sigma_x^2 = 2Dt = \frac{4\varepsilon L}{3qE}. \quad (1.6)$$

281 The minimal diffusion width is given by the lowest possible energy of the particles
 282 $\varepsilon_{\text{th}} = \frac{3}{2}kT$ (corresponding to thermal motion):

$$\sigma_{x, \text{min}}^2 = \frac{2kTL}{qE}. \quad (1.7)$$

283 For electrons in "cold gases" (e.g., Ar/CO₂ mixture), the diffusion approaches
284 this limit up to a certain field intensity (~ 100 V/cm at 1 atm pressure)¹. In
285 reality, the transversal diffusion of electrons can differ significantly from their
286 longitudinal diffusion and simulations are necessary to get a precise result.

287 In most TPCs, the transversal (but not the longitudinal) diffusion is reduced
288 by the magnetic field, since it is parallel to the electric field and curves the dif-
289 fusing electrons around their mean trajectory:

$$\frac{D_T(B)}{D_T(0)} = \frac{1}{C + \omega^2 \tau_2^2}, \quad (1.8)$$

290 where C and τ_2 are parameters dependent on the gas used. At low intensity of
291 the magnetic field, we can use an approximation $C \approx 1$ and $\tau_2 \approx \tau$.

292 1.2 Readout

293 1.2.1 Multi-Wire Proportional Chamber

294 In most (2010 – almost all) TPCs operated in experiments Multi-Wire Proport-
295ional Chamber (MWPC) (actually wire chamber? – similar? seems like it can
296 be used for readout, e.g., CERES) was used for the readout. The electrons enter
297 the chamber through a cathode grid and get accelerated in the strong electric
298 field towards the thin anode wires and create a Townsend avalanche (ref), mul-
299 tiplying the signal. Alternating with field wires? That is the difference between
300 MWPC and a drift chamber? The trajectory can be reconstructed using signal
301 from each separate wire. Segmented cathode is also often used for the readout of
302 produced cations. Gating grid (reduction of space charge effect, blocking backflow
303 of ions?, closed for electrons B=0, ΔV , static mode (loss of 25% el.) x opening on
304 trigger)? (gas amplification > 10000 required for good SNR, 100-200 ns shaping
305 time), figure – field (acts as a plane from far away and the field only gets strong
306 enough for avalanches)?

307 1.2.2 Gas Electron Multiplier

308 A Gas Electron Multiplier (GEM) is a thin metal-coated polymer sheet with
309 a high density of small holes (Figure 1.3). The amplification is achieved by ap-
310 plying voltage on the metal layers, creating a strong electric field inside the holes
311 and causing avalanches (see Figure 1.4). Double or triple stack of GEMs is usu-
312 ally used to create a sufficient gain. From the last foil, the electrons drift to
313 a segmented anode where the signal is read. The backflow of cations is reduced
314 compared to MWPC. Typical parameters (vs thick GEM?).

315 1.2.3 Micromegas

316 In a MICRO-MEsh GAseous Structure (Micromegas) (in sources I viewed it is not
317 capitalized) electrons pass through a fine mesh (made out of very thin wires) into

¹For us $\sigma_{x, \min} = 0.45$ mm, quite close to the actual diffusion 0.5-0.7 mm – details of the calculation.

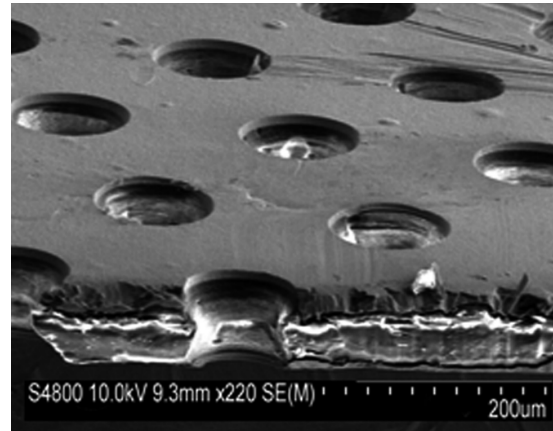


Figure 1.3: A scanning electron microscope image of a GEM foil [27].

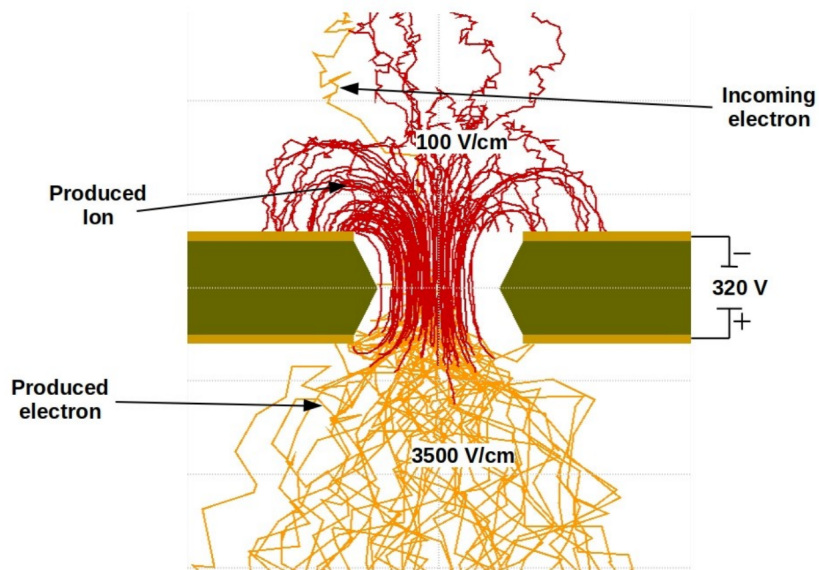


Figure 1.4: Garfield simulation of an avalanche in a GEM hole [28]. An incoming electron (orange) is accelerated in the strong electric field of the GEM and causes further ionization multiplying the number of free electrons (orange). Most of the produced cations (red) are captured by the GEM cathode.

318 the narrow amplification gap where they are multiplied in the high field and read
319 as signal on the segmented anode. Very high field ($30\text{-}80 \text{ kV/cm}^2$) is necessary
320 to achieve sufficient gain. Cation backflow is heavily suppressed by the mesh.

321 1.2.4 Parallel Plate Chamber

322 ... micowell? – these readouts and Micromegas are not used in our detector,
323 so maybe just mention them at the beginning of the readout section without
324 excessive detail (some subfigures showing how they look without describing each
325 too much)

326 1.3 Orthogonal Fields TPC at IEAP CTU

327 At IEAP CTU, we are going to use six identical atypical TPCs with inhomogeneous
328 toroidal magnetic field **orthogonal** to the electric field (**details below**),
329 hereafter referred to as Orthogonal Fields TPC (OFTPC). It has the shape of
330 isosceles trapezoidal prism 16 centimeters high with triple-GEM readout on one
331 of its bases. Dimensions of the OFTPC are discussed in detail in section 1.3.2
332 below. Throughout this thesis, we assume a uniform electric field along the z axis
333 with $E_z = -400 \text{ V/cm}$. Isn't the field affected by the MWPCs? Eventually a sim-
334 ulation will be needed. Measured particles enter the OFTPC through a window
335 after crossing the MWPC. Gas mixture used in the detector (70/30) and its effect
336 – some graph with the mixture. Argon used because of price (helium better for
337 multiple scattering)? Add a figure of the real TPC.

338 1.3.1 Motivation and Associated Challenges

339 The reasons for the unusual field layout are mostly cost related:
340 a) we use permanent magnets instead of a solenoid and parallel fields are
341 difficult to accomplish this way,
342 b) granularity of the TPC readout is limited in order to fit one SAMPA/SRS
343 hybrid in each sector – parallel fields would bend the trajectories parallel
344 to the readout requiring more pads and different architecture.

345 In this thesis, we will show that such a setup can reach a similar energy resolution
346 as common cylindrical TPCs while reducing the overall cost.

347 The layout introduces two complications to the track reconstruction – the
348 trajectory in inhomogeneous field is not circular and the drift is distorted by the
349 magnetic field as shown in the Equation 1.1(in our case $\omega\tau \approx 0.08$ for 0.3 T
350 assuming $\mu \approx 0.25 \text{ T}^{-1}$, varies inside the detector). We will deal with these
351 effects in the upcoming chapters.

352 The diffusion in such setup is larger since parallel orientation reduces diffu-
353 sion by curling the electrons in the $x\text{-}y$ direction (see Equation 1.8), but for our
354 relatively weak magnetic field and short drift distance, the difference is negligible.

355 1.3.2 Coordinate Systems and Dimensions

356 In order to describe events in our detector, we use three distinct spaces: the de-
357 tector space \mathcal{D} , the readout space \mathcal{R} and the pad space \mathcal{P} (**different spaces that**

358 describe different things and each has their own coordinate system, so maybe
 359 rename the section somehow?). Each space is later used to represent ionization
 360 electrons at different stages of the detection process: their creation in the gas,
 361 their final position when hitting the readout plane, and finally their representation
 362 in the discrete pad space.

363 Detector Space

364 The detector space \mathcal{D} represents the physical space of our detector. We de-
 365 scribe it using Cartesian coordinates (x, y, z) . The z -axis is the detector's axis of
 366 symmetry, with its negative direction aligned with the proton beam. The origin
 367 $(0, 0, 0)$ is located at the center of the irradiated target. The positive x -axis passes
 368 through the center of one the OFTPCs along the intersection of its two planes
 369 of symmetry. The y -axis is then chosen to maintain a right-handed coordinate
 370 system.

371 Since the detector has a hexagonal symmetry, we use only one of its sectors
 372 in this work – the first sector $\mathcal{D}_1 \subset \mathcal{D}$ which is defined by the condition:

$$(x, y, z) \in \mathcal{D}_1 \Leftrightarrow |y| \leq x \tan \frac{\pi}{6}. \quad (1.9)$$

373 Simulations in this sector can be applied to all sectors by rotating the coordinates
 374 accordingly. The volume of the OFTPC in this sector, which has the shape of
 375 a trapezoidal prism, has these boundaries:

$$x \in [x_{\min}, x_{\max}] = [6.51, 14.61] \text{ cm}, \quad (1.10)$$

$$z \in [z_{\min}, z_{\max}] = [-8, 8] \text{ cm}, \quad (1.11)$$

$$y_{\max}(x_{\min}) = -y_{\min}(x_{\min}) = 2.75 \text{ cm}, \quad (1.12)$$

$$y_{\max}(x_{\max}) = -y_{\min}(x_{\max}) = 7.45 \text{ cm}, \quad (1.13)$$

376 where $y_{\max}(x)$ is the maximal value of the y -coordinate for a given x . The read-
 377 out is located at $z = 8$ cm; for some purposes, we also define the distance to
 378 the readout $d_r = 8 \text{ cm} - z$ as an alternative to the z -coordinate. Keeping this
 379 paragraph as it is because the OFTPC volume is distinct from the first sector
 380 and some parts of this thesis use the space beyond this volume. The OFTPC
 381 window has width 3.8 cm and height 4.0 cm.

382 We also use spherical coordinates (r, θ, φ) with the elevation angle θ measured
 383 relative to the xy plane. Angles θ and φ are useful when describing the direction
 384 of e^+ / e^- tracks. Their maximal values considered for the initial direction in
 385 simulations are $\theta_{\max} \approx 17.1^\circ$ and $\varphi_{\max} \approx 16.3^\circ$ as shown in Figure 1.5.

386 Readout Space

387 The readout space \mathcal{R} represents the drift time and final positions of ionization
 388 electrons as measured by an ideal continuous readout. We describe it using
 389 coordinates (x', y', t) , where x' and y' correspond to the detector coordinates at
 390 the readout plane ($z = 8$ cm).

391 Currently not entirely sure how to put this into a figure since only x' and
 392 y' correspond to the detector coordinates, it will make more sense when
 393 visualizing the map. The drift time t is approximately proportional to d_r .

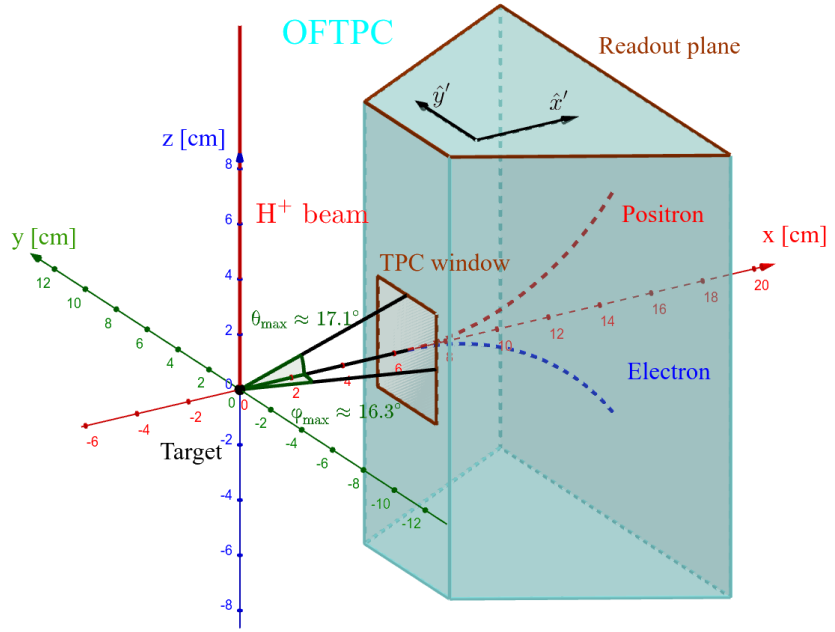


Figure 1.5: Schematics of the first sector OFTPC with detector space coordinates.

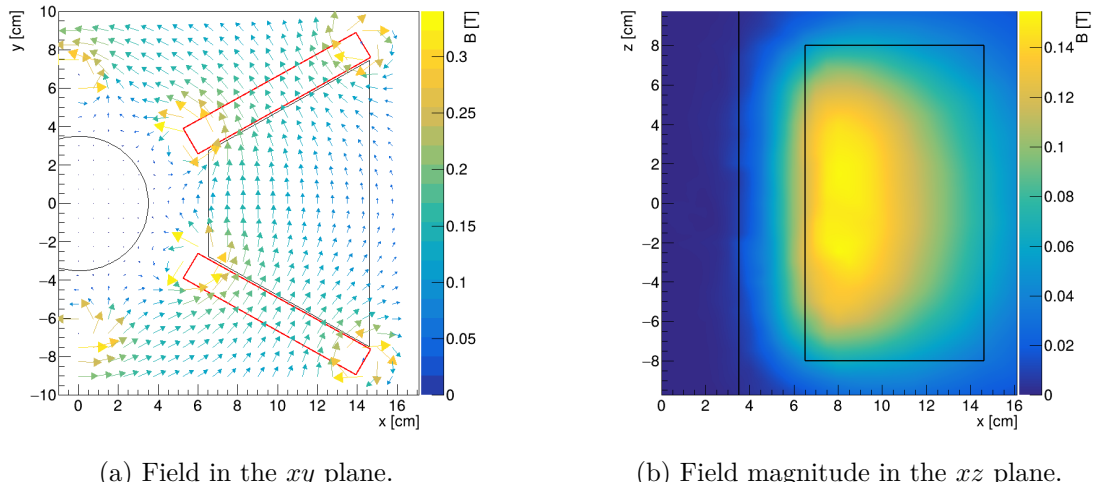
394 Pad Space

395 The pad space \mathcal{P} represents the time bin and pad number of ionization electrons
 396 as measured by an ideal discrete readout:

$$\mathcal{P} = \{(n_{\text{pad}}, n_t) \in \mathbb{N}^2 \mid n_{\text{pad}} \leq 128\}. \quad (1.14)$$

397 **Rewrite to reflect this:** Technically both values can be zero as defined in
 398 the code (max channel 127). It is not really a subspace of \mathcal{R} but there is a
 399 mapping from \mathcal{R} to \mathcal{P} . It is a discretization of a part of \mathcal{R} , the mapping can be
 400 adjusted depending on the simulation. If we assume uniform electric field there
 401 will be gaps, we don't use gaps in the reconstruction since the electrons should
 402 be pulled towards the pads.

403 The readout of the OFTPC will consist (is the design final?) of 128 rectangular
 404 pads arranged in a staggered pattern. Parameters of the pad layout are shown
 405 in Figure 1.6. The bottom left corner of n -th pad has coordinates $(x_{1,n}, y_{1,n})$,
 406 the top right $(x_{2,n}, y_{2,n})$ and its center has coordinates $(x_{c,n}, y_{c,n})$. The gap
 407 between neighboring pads is $g = 0.08$ cm. Time will be read out in discrete bins
 408 of size $t_{\text{bin}} = 100$ ns (details?). Could also describe pad-related functions.



(a) Field in the xy plane.

(b) Field magnitude in the xz plane.

Figure 1.7: Magnetic field simulation results. The OFTPC volume and the vacuum tube are marked with black lines, the magnets are marked with red lines. The coordinates of the magnets from the CAD drawing seem to be 9/10 of the ones from the magnetic simulation (confirm and fix).

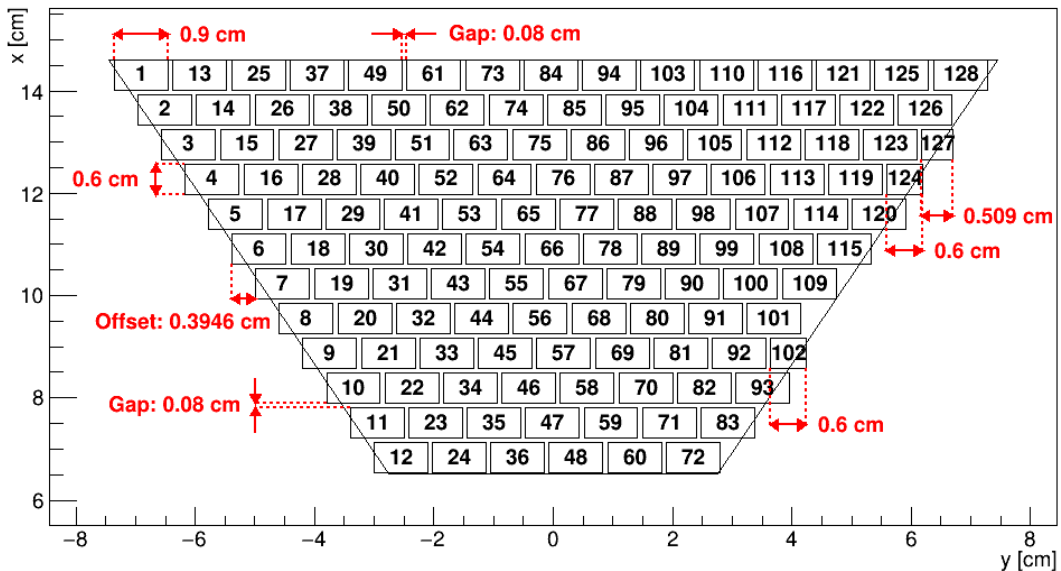


Figure 1.6: Pad layout of the OFTPC and its parameters. Pads 102, 124 and 127 are irregular, the rest has the same dimensions.

409 1.3.3 Magnetic Field Simulation

410 The magnetic field inside our detector is produced by six permanent magnets. It
 411 was simulated using Ansys Maxwell ([citation](#)) which gives us values on a regular
 412 grid. More details, vacuum tube, magnets (homogeneous?, density?). Visualization
 413 of the magnetic field is shown in Figure 1.7. Whenever we need to work with
 414 values outside this grid, we use trilinear interpolation described below.

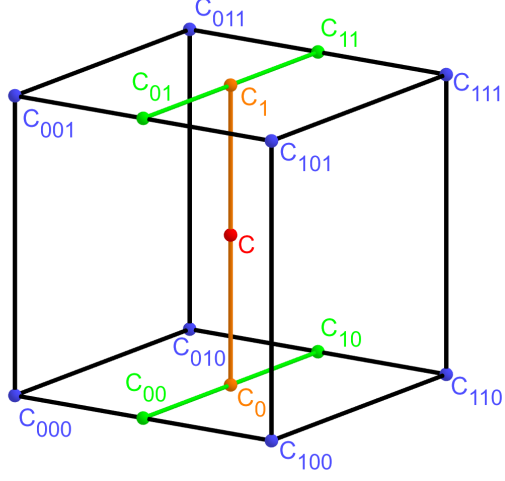


Figure 1.8: Visualization of trilinear interpolation as a composition of linear interpolations (inspired by [29]). We want to interpolate the value in the red point \mathbf{C} . First we interpolate between the four pairs of blue points sharing the last two indices along the x -axis (Eq. 1.15), then between the two pairs of the resulting green points along the y -axis (Eq. 1.16) and finally between the two resulting orange points along the z -axis to get the final red value (Eq. 1.17).

415 Trilinear Interpolation

416 Trilinear interpolation is a 3D generalization of linear interpolation². It can be
 417 used to interpolate a function whose values are known on a regular grid with
 418 rectangular prism cells. We use this simple method for interpolating the magnetic
 419 field, and it is later used in Section 3.2.1 to interpolate the Ionization Electron
 420 Map, a key component of our track reconstruction algorithm. In both cases, we
 421 use a regular cubic grid (apparently it is also called a **Cartesian grid**).

422 Let us consider a cell of our regular grid (a cube) with an edge of length a
 423 containing the point $\mathbf{C} = (x, y, z)$ where we want to interpolate a function
 424 $f: \mathbb{R}^3 \rightarrow \mathbb{R}$. We know the values of this function at the vertices of the cell $\mathbf{C}_{ijk} =$
 425 $= (x_0 + ia, y_0 + ja, z_0 + ka)$, where $\mathbf{C}_{000} = (x_0, y_0, z_0)$ is the origin of the cell (is
 426 that clear?), and $i, j, k \in \{0, 1\}$ are indices. We also define the points $\mathbf{C}_{ij} =$
 427 $= (x, y_0 + ia, z_0 + ja)$ and $\mathbf{C}_i = (x, y, z_0 + ia)$. Then the interpolated value $\hat{f}(\mathbf{C})$
 428 can be calculated as a composition of three linear interpolations (see Figure 1.8):

$$\hat{f}(\mathbf{C}_{ij}) = (1 - x_d) f(\mathbf{C}_{0ij}) + x_d f(\mathbf{C}_{1ij}), \quad (1.15)$$

$$\hat{f}(\mathbf{C}_i) = (1 - y_d) \hat{f}(\mathbf{C}_{0i}) + y_d \hat{f}(\mathbf{C}_{1i}), \quad (1.16)$$

$$\hat{f}(\mathbf{C}) = (1 - z_d) \hat{f}(\mathbf{C}_0) + z_d \hat{f}(\mathbf{C}_1), \quad (1.17)$$

429 where x_d , y_d , and z_d are given as follows:

$$x_d = \frac{x - x_0}{a}, \quad y_d = \frac{y - y_0}{a}, \quad z_d = \frac{z - z_0}{a}. \quad (1.18)$$

²Linear interpolation in point $x \in (x_1, x_2)$ of a function $f: \mathbb{R} \rightarrow \mathbb{R}$ known in points $x_1 < x_2$ is the convex combination $\hat{f}(x) = (1 - x_d)f(x_1) + x_d f(x_2)$, where $x_d = \frac{x - x_1}{x_2 - x_1} \in (0, 1)$.

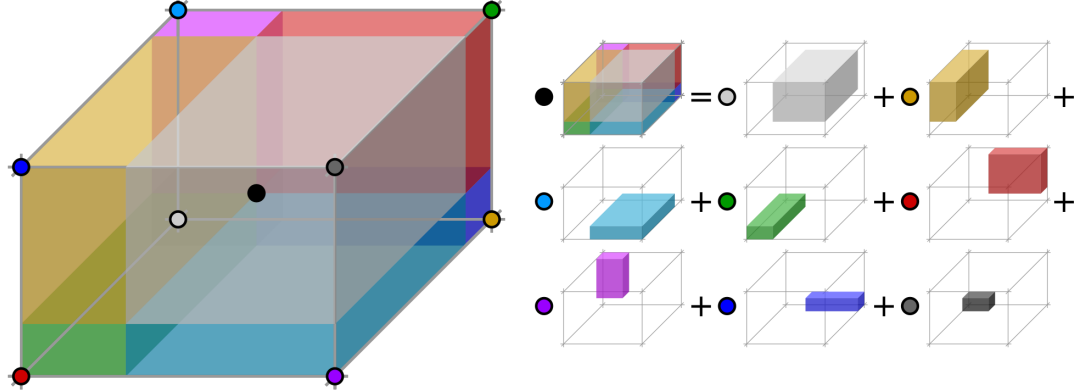


Figure 1.9: Geometric interpretation of trilinear interpolation as expressed in Equation 1.19. The colored dots represent the values in given points and the colored boxes represent the volume in the opposite corner by which the corresponding values are multiplied. The black dot represents the interpolated value which is multiplied by the entire volume [30].

430 We can also write

$$\hat{f}(\mathbf{C}) = \sum_{i,j,k \in \{0,1\}} t_x^i t_y^j t_z^k f(\mathbf{C}_{ijk}), \quad (1.19)$$

$$t_\alpha \stackrel{\text{def}}{=} \begin{pmatrix} t_\alpha^0 \\ t_\alpha^1 \end{pmatrix} = \begin{pmatrix} 1 - \alpha_d \\ \alpha_d \end{pmatrix}, \quad (1.20)$$

431 where $\alpha \in \{x, y, z\}$ is an index. This gives a nice geometric interpretation to the
432 trilinear interpolation as shown in Figure 1.9. From this form and the figure, it
433 is apparent that the final interpolated value does not depend on the order of axes
434 along which we perform linear interpolations (see Figure 1.8). Furthermore, we
435 can write $\hat{f}(\mathbf{C})$ as a polynomial:

$$\hat{f}(\mathbf{C}) = \sum_{\alpha,\beta,\gamma \in \{0,1\}} \sum_{i=0}^{\alpha} \sum_{j=0}^{\beta} \sum_{k=0}^{\gamma} (-1)^{(\alpha-i)+(\beta-j)+(\gamma-k)} f(\mathbf{C}_{ijk}) x_d^\alpha y_d^\beta z_d^\gamma. \quad (1.21)$$

436 We take advantage of this form when generalizing trilinear interpolation to irregular
437 grid in section 3.2.2.

438 Maybe a citation here, although I am not sure it is necessary since it could
439 be considered common knowledge. The last two equations are my own (but I'm
440 not sure that's worth mentioning unless there's a citation).

2. Track Simulation

In order to develop and test the reconstruction algorithm, electron and positron tracks are simulated inside the first detector sector \mathcal{D}_1 (see Section 1.3.2) with different initial parameters (origin, initial direction and kinetic energy). Two approaches are currently used to simulate tracks, each of them for different purpose.

The **Microscopic Simulation** uses the Garfield++ toolkit [1]. Within this toolkit:

- a) Magboltz, since it is mentioned later
- b) the High Energy Electro-Dynamics (HEED) program [31] is used to simulate the primary particle,
- c) the class *AvalancheMicroscopic* to simulate the drift of secondary electrons created by ionization in the gas.

This is the most precise and time-consuming simulation used; our current goal is to be able to successfully reconstruct its results and determine our best-case energy resolution.

The **Runge-Kutta Simulation** uses the 4th order Runge-Kutta numerical integration (add citation for Runge-Kutta) to simulate the trajectory of the primary particle in the electromagnetic field inside the detector. It is relatively fast since it does not simulate the secondary particles. It is used as part of our reconstruction algorithm and for testing some parts of the reconstruction.

All of these simulations require the knowledge of the electromagnetic field (both **E** and **B**) inside the detector. A uniform electric field of $400 \text{ V}\cdot\text{cm}^{-1}$ is assumed. The magnetic field was simulated in Maxwell (see Section 1.3.3). add citation

Single track in positive x direction or initial parameter randomization. Importance of gas composition, used gas compositions.

2.1 Microscopic Simulation

The microscopic simulation, the most detailed simulation used in this work, is performed using the Garfield++ toolkit [1].

The electron transport properties are simulated using the program Magboltz (add citation), (details?). Two different gas mixtures were compared – 90:10 and 70:30 Ar:CO₂. The second mixture will be used in our detector (this was probably known a priori, but the first tests that I started with used 90/10, so maybe just note that the results justify the fact so far). The temperature is set to 20 °C, the pressure is atmospheric.

The primary track is simulated using the program HEED, which is an implementation of the photo-absorption ionization model [31] (see the reference, moved it to the end of sentence). This program provides the parameters of ionizing collisions. HEED can also be used to simulate the transport of delta electrons; we do not account for these in the current simulation (but plan to include them in the future – maybe mention only in the conclusion/future section). The photons created in the atomic relaxation cascade (fluorescence reabsorption, related to the spread of avalanches in GM det.?) are also not simulated.

484 Finally, we use the microscopic tracking provided by the class *AvalancheMicroscopic*
 485 in Garfield++ to simulate the drift of the ionization electrons. Each
 486 electron is followed from collision to collision using the equation of motion and
 487 the collision rates calculated by Magboltz.

488 Add more detailed and better description of HEED, and microscopic tracking
 489 (each their own subsection?). Could also mention Monte Carlo (requires gas file
 490 generation - Magboltz) and Runge-Kutta simulation implemented in Garfield,
 491 why we don't use them (another subsection? rename the section to Garfield++
 492 simulation and mention all relevant parts?).

493 2.1.1 First testing track

494 The first electron track simulated for testing purposes was chosen to have a special
 495 set of parameters:

- 496 • the starting point of the track is the origin of the coordinate system,
- 497 • the initial direction is along the positive x -axis,
- 498 • the momentum is 8 MeV/c (the kinetic energy is 7.505 MeV).

499 Such a track moves in the XZ plane in the toroidal magnetic field of the detector,
 500 because the particle's velocity vector is always perpendicular to the field. At first,
 501 we simulated such a track in 90:10 Ar:CO₂ gas mixture, later we added a simu-
 502 lation in 70:30 Ar:CO₂, which we plan to use in our detector. The comparison of
 503 both simulations is in Figure 2.1.

504 2.1.2 Grid-like testing sample

505 In order to test all steps of the reconstruction, a sample of tracks with a grid-like
 506 distribution of parameters was generated on MetaCentrum. Five sets of 9702
 507 tracks were generated with every combination of these parameters:

- 508 • electron and positron tracks,
- 509 • 11 different kinetic energies $E_{\text{kin}} \in [3, 13]$ MeV,
- 510 • 21 different azimuth angles $\varphi \in [-16.3^\circ, 16.3^\circ]$ and
- 511 • 21 different elevation angles $\theta \in [-17.1^\circ, 17.1^\circ]$.

512 A visualization of a set of e^+/e^- tracks with the same kinetic energy is shown
 513 in Figure 2.2 (plotting actual HEED tracks using ROOT should be also possible
 514 (but hard to make look good?)). In the 70:30 Ar:CO₂ atmosphere, each track
 515 takes 5-30 CPU hours to simulate. Every tenth point on the drift line was stored,
 516 the whole sample has 3.1 terabytes (or 1.4 gigabytes without drift lines).

517 2.2 Runge-Kutta Simulation

518 The Runge-Kutta simulation in this work uses the Runge-Kutta 4th order (RK4)
 519 method to numerically integrate the equation of motion of a relativistic charged
 520 particle in an electromagnetic field. Given a system of first order differential
 521 equations

$$\frac{dy}{dt} = \mathbf{f}(t, \mathbf{y}(t)) \quad (2.1)$$

522 with an initial condition

$$\mathbf{y}(t_0) = \mathbf{y}_0, \quad (2.2)$$

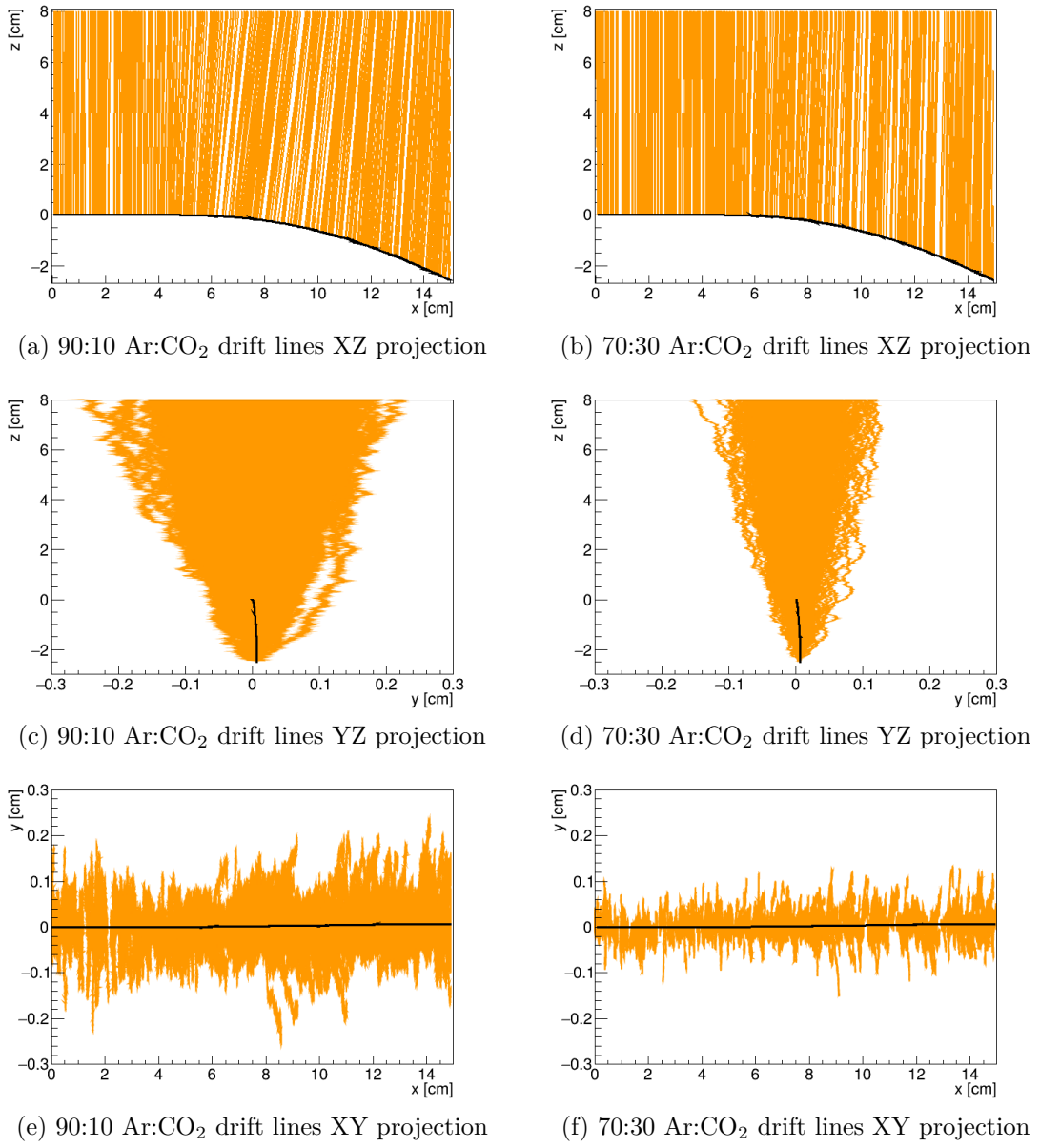


Figure 2.1: Comparison of drift lines for two different gas mixtures 90:10 and 70:30 Ar:CO₂. The electron track is marked in black, the drift lines of the ionization electrons are marked in orange. In this example, we assume a larger OFTPC volume with readout at $z = 8$ cm.

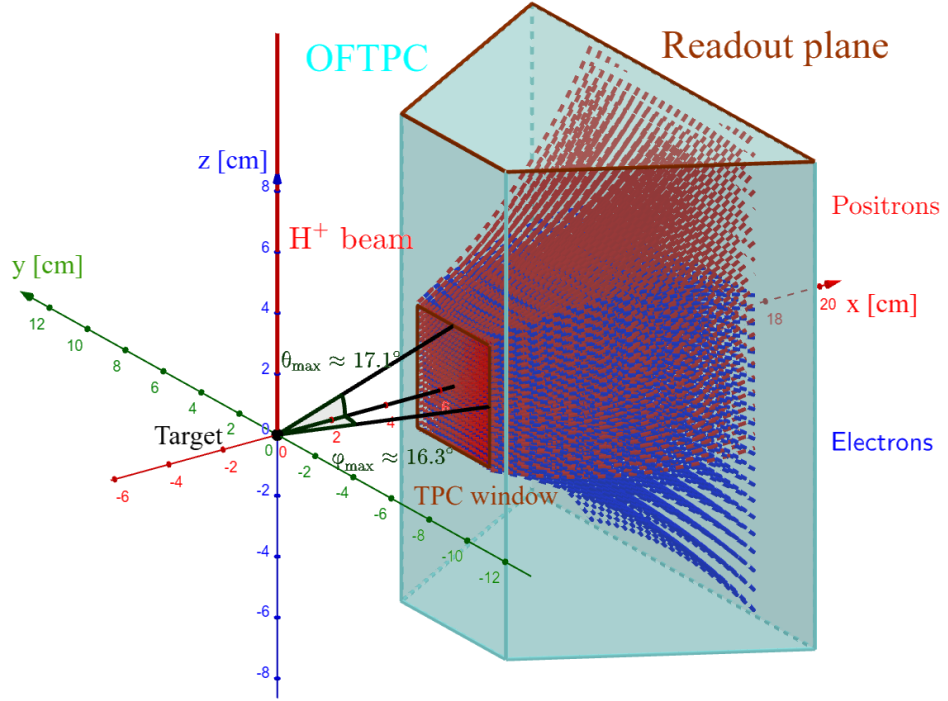


Figure 2.2: A visualization of a set of tracks from the grid-like testing sample with the same kinetic energy.

523 we iteratively compute the estimate $\mathbf{y}_n = \mathbf{y}(t_n) = \mathbf{y}(t_0 + nh)$ as follows (citation?
 524 common knowledge?):

$$\mathbf{k}_1 = \mathbf{f}(t_n, \mathbf{y}_n), \quad (2.3)$$

$$\mathbf{k}_2 = \mathbf{f}\left(t_n + \frac{h}{2}, \mathbf{y}_n + \frac{h\mathbf{k}_1}{2}\right), \quad (2.4)$$

$$\mathbf{k}_3 = \mathbf{f}\left(t_n + \frac{h}{2}, \mathbf{y}_n + \frac{h\mathbf{k}_2}{2}\right), \quad (2.5)$$

$$\mathbf{k}_4 = \mathbf{f}(t_n + h, \mathbf{y}_n + h\mathbf{k}_3), \quad (2.6)$$

525

$$\mathbf{y}_{n+1} = \mathbf{y}_n + \frac{1}{6}(\mathbf{k}_1 + 2\mathbf{k}_2 + 2\mathbf{k}_3 + \mathbf{k}_4). \quad (2.7)$$

526 Alternate forms (infinitely many) possible, accuracy vs computational cost. Runge-
 527 Kutta-Fehlberg with adaptive step size also possible, can potentially save some
 528 computation time especially in rapidly changing field (so maybe not in this case).

529 In our case, we want to integrate the equation of motion, given by the rela-
 530 tivistic Lorentz force:

$$F_L^\mu = m \frac{du^\mu}{d\tau} = q F^{\mu\nu} u_\nu, \quad (2.8)$$

531 where the Einstein summation convention is used, m is the mass of the particle,
 532 q is its charge, u^μ is its four-velocity, τ is the proper time (i.e., time in the particle's
 533 frame of reference) and $F^{\mu\nu}$ is the electromagnetic tensor at given coordinates x^μ
 534 (we consider it to be time-independent in our detector). Given the electric $\mathbf{E} =$
 535 $= (E_x, E_y, E_z)$ and the magnetic field $\mathbf{B} = (B_x, B_y, B_z)$ and using the metric

536 signature $(+, -, -, -)$, the equation expands to

$$\frac{d}{d\tau} \begin{pmatrix} \gamma c \\ \gamma v_x \\ \gamma v_y \\ \gamma v_z \end{pmatrix} = \frac{q}{m} \begin{pmatrix} 0 & -\frac{E_x}{c} & -\frac{E_y}{c} & -\frac{E_z}{c} \\ \frac{E_x}{c} & 0 & -B_z & B_y \\ \frac{E_y}{c} & B_z & 0 & -B_x \\ \frac{E_z}{c} & -B_y & B_x & 0 \end{pmatrix} \begin{pmatrix} \gamma c \\ \gamma v_x \\ \gamma v_y \\ \gamma v_z \end{pmatrix}, \quad (2.9)$$

537 where c is the speed of light in vacuum, $\mathbf{v} = (v_x, v_y, v_z)$ is the particle's velocity
 538 and $\gamma = (1 - \frac{v^2}{c^2})^{-\frac{1}{2}}$ is the Lorentz factor (wrong magnetic field sign in the
 539 implementation???). Together with the equation

$$\frac{d}{d\tau} \begin{pmatrix} ct \\ x \\ y \\ z \end{pmatrix} = \begin{pmatrix} \gamma c \\ \gamma v_x \\ \gamma v_y \\ \gamma v_z \end{pmatrix} = u^\mu, \quad (2.10)$$

540 we get a system of eight first order differential equations for x^μ and u^μ , which
 541 we can integrate using the Runge-Kutta method described above. As a result of
 542 this integration, we get the position $\mathbf{x}(\tau_n)$, the velocity $\mathbf{v}(\tau_n)$ and the detector
 543 time $t(\tau_n)$ for every proper time $\tau_n = n\tau_{\text{step}}$. Integrating using the proper time
 544 means that the step size in t gets larger by the gamma factor $\frac{dt}{d\tau} = \gamma$ (maybe
 545 change it and integrate the detector time or adjust the step size accordingly). The
 546 only difference is in the step size (because t gets also calculated as it is among the
 547 8 variables). It might be even better to adjust the step size using approx-
 548 imate distance traveled. As initial conditions, we use the origin of the track
 549 (x_0, y_0, z_0), the initial velocity direction vector $\mathbf{n} = (\cos \varphi \cos \theta, \sin \varphi \cos \theta, \sin \theta)$
 550 and the kinetic energy E_{kin} (initial parameters of the simulation (fit is in chap-
 551 ter 4)), we then compute γ and $\|\mathbf{v}\|$:

$$\gamma = 1 + \frac{E_{\text{kin}}}{E_0}, \quad (2.11)$$

$$\|\mathbf{v}\| = c\sqrt{1 - \gamma^{-2}}. \quad (2.12)$$

552 2.2.1 Testing sample

553 Example of RK simulation – first testing track, randomized sample of 100000
 554 tracks (could also move them to circle 3D fit).

555 In order to test the simulation and reconstruction, a sample of 100 000 tracks
 556 with randomized parameters was generated:

- 557 the Runge-Kutta step was set to 0.1 ns (proper time, which wouldn't be a
 558 problem but this way the "spatial" step depends on energy),
- 559 the kinetic energy of the particle $E_{\text{kin}} \in [4, 12]$ MeV,
- 560 the starting point of the track is a random point in the OFTPC window,
- 561 the initial direction is given by the line connecting a random point on
 562 the target¹ (a disc with 1 mm radius in the YZ plane).

¹To generate a random point on the target, we generate a random angle α and a random square of the distance from origin r^2 to get a uniform distribution.

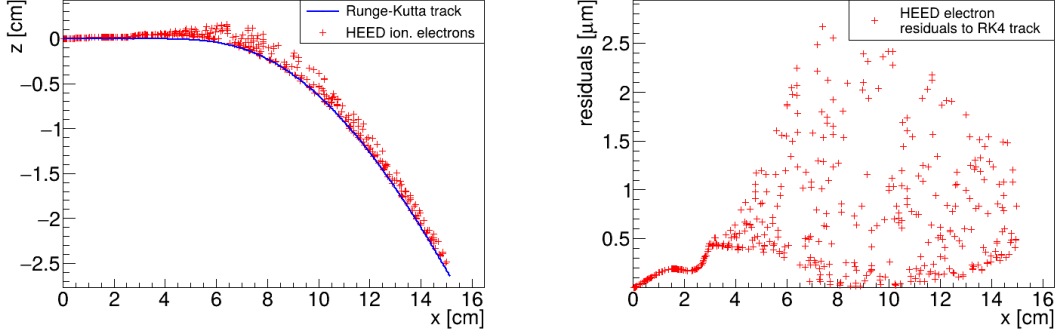


Figure 2.3: A comparison of the HEED track from the microscopic simulation in Section 2.1.1 with a Runge-Kutta track with the same initial parameters and $\tau_{\text{step}} = 0.1$ ps (reducing the step further doesn't make a visible difference). In the view of the tracks on the left, the distance of the HEED ionization electrons from the RK4 track is exaggerated 1000 \times . On the right, the dependence of the HEED electrons residuals (i.e., their shortest distance to the RK4 track) on their z -coordinate is shown. The images look the same even for 100,000x smaller step, so the residuals are a result of something that HEED does (maybe a different interpolation technique for the magnetic field? the pattern looks similar for two different tracks so it can't be scattering).

When exaggerating, the HEED ionization electrons are moved away along the shortest line connecting them to the RK4 track. The computation of this distance is described in Section 4.3.

- 563 Since the Runge-Kutta simulation is quite fast², it can be run locally on any
 564 computer. Add a figure with simulated tracks (sample). An example Runge-
 565 Kutta track is compared with the corresponding microscopic track in Figure 2.3.

²One track with $\tau_{\text{step}} = 0.1$ ps takes less than one millisecond to simulate.

3. Track Reconstruction

As the first step of the reconstruction algorithm, we reconstruct the track of a primary particle – either an electron or a positron. Then, using this information, we determine the energy of the particle (Section 4).

The **Reconstruction Assuming Steady Drift** uses the standard TPC approach. With parallel fields, the drift inside a uniform electric field remains undistorted (as shown in Equation 1.1). Therefore, we only need to reconstruct the z -coordinate from the drift time using the known drift velocity. We also assume that the readout coordinates (x' , y' , t) are known exactly, neglecting the pads and time binning.

Reconstruction using an **Ionization Electron Map** (from now on referred to as *the map*) uses a simulation of the drift of secondary (ionization) electrons within the detector volume. This simulation can then be used to interpolate the initial position of the secondary electrons. In the first iteration of this method the readout is assumed to be continuous.

We present two algorithms using the map for reconstruction. The first one uses a gradient descent algorithm along with trilinear interpolation (see Section 1.3.3) of the map. The second method uses interpolation on the irregular inverse grid with a polynomial.

The **Discrete Reconstruction** uses the map; instead of reconstructing the exact position of each electron, we reconstruct the center of each hit pad together with the time corresponding to the midpoint of the time bin. The electron count in each TPC bin (consisting of the pad and the time bin) serves as an idealized collected charge, which is then used as a weight in the energy reconstruction fit.

3.1 Reconstruction Assuming Steady Drift

As the first step, we tried to reconstruct a simulated electron track with a special set of initial parameters, described in detail in Section 2.1.1. The starting point is given by the origin of our coordinate system and its initial direction is given by the positive x -axis. This means the magnetic field of our detector is perpendicular to the momentum of the particle at all times, and we can reduce the problem to two-dimensional space.

For the reconstruction, we decided to use the common method used in a standard TPC (similar to?, cite some source(s)!). This will allow us to explore the significance of the atypical behavior in our OFTPC. Additionally, we assume the readout is continuous to further simplify the problem. In this approximation, we reconstruct the initial position of each ionization electron.

The reconstruction is then defined by the following relations between the coordinates of the detector space and the readout space (see Section 1.3.2):

$$x = x', \tag{3.1}$$

$$y = y', \tag{3.2}$$

$$z = 8 \text{ cm} - d_r = 8 \text{ cm} - v_d t, \tag{3.3}$$

where d_r is the distance to the readout, and v_d is the drift velocity of electrons in the given gas mixture. At a phenomenological level, this velocity can be con-

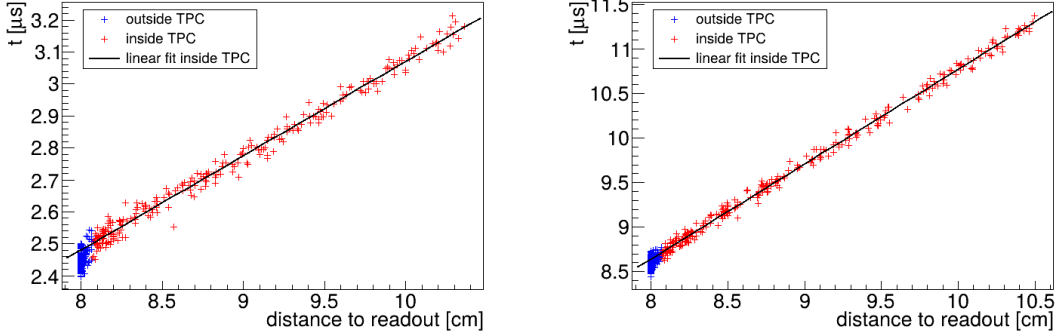


Figure 3.1: Linear fit of the drift time t dependence on the distance to the readout $d_r = 8 \text{ cm} - z$ for the ionization electrons in 90:10 (left) and 70:30 (right) Ar:CO₂ gas composition. Only electrons inside the TPC (red) are fitted. The parameters are $v_d = 3.39 \text{ cm}/\mu\text{s}$, $d_0 = -0.41 \text{ cm}$ for 90:10, and $v_d = 0.939 \text{ cm}/\mu\text{s}$, $d_0 = -0.11 \text{ cm}$ for 70:30 Ar:CO₂.

sidered as a function of the electric field \mathbf{E} and the magnetic field \mathbf{B} as shown in Equation 1.1. The Garfield++ toolkit uses this fact to accelerate their drift simulation with non-microscopic approaches (could mention in the simulation chapter). Since we assume a uniform electric field in the detector and in this approximation we want to neglect the effect of our unusual magnetic field, we consider the drift velocity constant. We can estimate the drift velocity by fitting the dependence $d_r(t)$ of ionization electrons from a simulated track with a linear function:

$$d_r(t) = v_d t + d_0. \quad (3.4)$$

The fit was applied on two tracks with different gas composition, the result is in Figure 3.1. Compare with real drift velocities – a good indication of the tilt of drift lines. The obtained parameters are then used for the reconstruction shown in Figure 3.2. From the residuals shown in Figure 3.3, we can see that this reconstruction algorithm leads to significant deviations from the simulated track (up to 1.1 cm for 90:10, and up to 0.3 cm for 70:30 Ar:CO₂), especially in the faster gas mixture 90:10 (as expected – for a higher mean time between collisions in Equation 1.1, the effect of the magnetic field is bigger). These deviations are mainly caused by the shift in the x -coordinate due to the tilt of the drift lines in magnetic field. In order to account for this, we need to develop a better algorithm. There is also a small irregularity in the z -coordinate but it is comparable with the diffusion. We can/will also later show that this has a significant effect on the reconstructed energy.

3.2 Ionization Electron Map

Inside an OFTPC (more than one, also considering it a general concept rather than the specific OFTPC used at this experiment), the drift of the ionization electrons is significantly affected by its magnetic field as shown in Equation 1.1, see also Figure 2.1. We need to take this into account for accurate reconstruction (should be easy to run the reconstruction without the map and show how much it improves the results). In the first approximation, we assume a continuous readout (i.e., we neglect the anode segmentation into pads). We can then

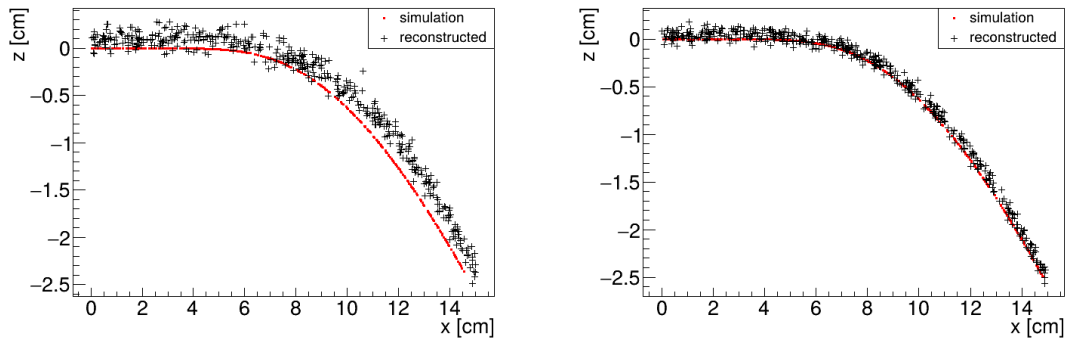


Figure 3.2: Reconstruction (black) of the starting position of ionization electrons (red) using parameters obtained from the fit (Figure 3.1). Two gas compositions 90:10 (left) and 70:30 Ar:CO₂ (right) are compared.

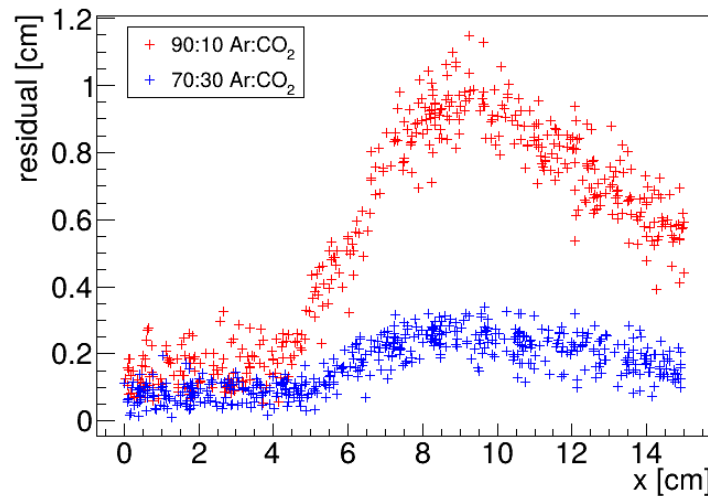


Figure 3.3: Comparison of residuals (i.e., the distance from the reconstructed point to the simulated ionization electron starting point) dependence on x for two gas mixtures 90:10 (red) and 70:30 Ar:CO₂ (blue).

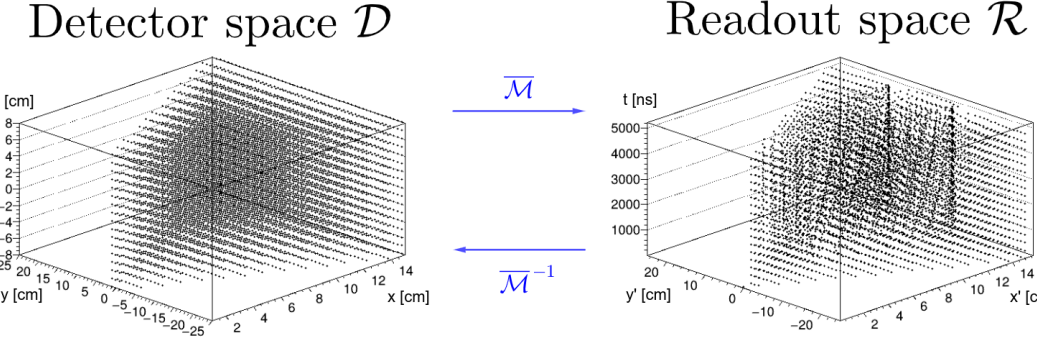


Figure 3.4: A 3D visualization of the mapping of means $\bar{\mathcal{M}}$ for the 90:10 Ar:CO₂ gas. A regular grid \mathbb{G} with $l = 1$ cm in the detector space is mapped to an irregular grid $\mathbb{G}^{-1} \equiv \bar{\mathcal{M}}(\mathbb{G})$ in the readout space.

634 reconstruct the original position of each ionization electron using its readout co-
635 ordinates. For this purpose, we use the ionization electron map.

636 The ionization electron map represents a mapping from the detector space
637 to the readout space (see Section 1.3.2). It tells us what readout coordinates
638 (x', y', t) we can expect on average for an ionization electron created at the detec-
639 tor coordinates (x, y, z). More precisely, it is a mapping to the distributions on
640 the readout space; we can simplify this as only the means $\bar{\mathcal{M}}$ and the covariance
641 matrices \mathcal{M}_Σ , assuming Gaussian distribution:

$$\bar{\mathcal{M}}: \mathcal{D} \longrightarrow \mathcal{R}, \quad (x, y, z) \longmapsto \bar{\mathbf{X}}^T \equiv (\bar{x}', \bar{y}', \bar{t}), \quad (3.5)$$

$$\mathcal{M}_\Sigma: \mathcal{D} \longrightarrow \mathbb{R}^{3 \times 3}, \quad (x, y, z) \longmapsto \Sigma \equiv \begin{pmatrix} \sigma_{x'}^2 & \text{cov}(x', y') & \text{cov}(x', t) \\ \text{cov}(y', x') & \sigma_{y'}^2 & \text{cov}(y', t) \\ \text{cov}(t, x') & \text{cov}(t, y') & \sigma_t^2 \end{pmatrix}, \quad (3.6)$$

$$\mathcal{M}: \mathcal{D} \longrightarrow D(\mathcal{R}), \quad (x, y, z) \longmapsto N(\mathbf{X}) \equiv \frac{\exp\left(-\frac{1}{2}(\mathbf{X} - \bar{\mathbf{X}})^T \Sigma (\mathbf{X} - \bar{\mathbf{X}})\right)}{\sqrt{(2\pi)^3 |\Sigma|}}. \quad (3.7)$$

642 To get an approximation of this mapping, we simulate the drift of ionization
643 electrons generated on a regular Cartesian grid $\mathbb{G} \subset \mathcal{D}$ with spacing l inside
644 the volume of our OFTPC¹ (see the visualization in Figure 3.4). In Figure 3.5, you
645 can see an example of drift lines from a test of the simulation. After testing runs,
646 two map simulations were made with different gas composition, their parameters
647 are shown in Table 3.1.

648 In order to get accurate results, we use the microscopic simulation of these
649 electrons described in Section 2.1 (Monte Carlo from *AvalancheMC* was also con-
650 sidered but it doesn't (didn't? CERES used it from MAGBOLTZ???) include
651 magnetic field, we can probably improve this anyway using the fast track sim-
652 ulation with map proposed in the future section). It is also useful to simulate
653 multiple (N) electrons originating from the same position so that we can account
654 for the random fluctuations due to collisions. Using the readout coordinates of
655 the electrons, we then estimate the means and the covariance matrix:

$$\bar{\mathbf{X}} = \frac{1}{N} \sum_{i=1}^N \mathbf{X}_i, \quad \Sigma = \frac{1}{N-1} \sum_{i=1}^N (\mathbf{X}_i - \bar{\mathbf{X}})(\mathbf{X}_i - \bar{\mathbf{X}})^T, \quad (3.8)$$

¹The detector walls are not considered and we simulate the drift even outside of the OFTPC which allows us to interpolate even close to the walls

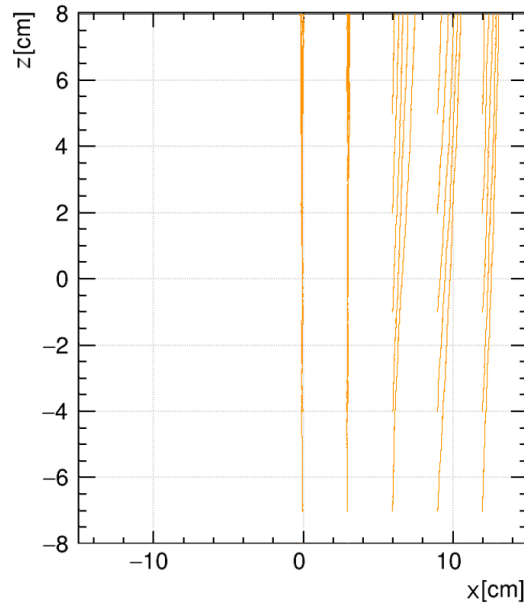


Figure 3.5: A test of the 90:10 Ar:CO₂ map simulation with spacing $l = 1.5$ cm. The resulting drift lines of evenly spaced electrons are displayed in orange.

Table 3.1: Comparison of parameters of two map simulations.

Parameter	90:10 Ar:CO ₂ map	70:30 Ar:CO ₂ map
N	100	100
l	1.0 cm	0.5 cm
z bounds	$[-8, 8]$ cm	$[-8, 8]$ cm
x bounds	$[0, 15]$ cm	$[-1.5, 15.0]$ cm
y bounds	$ y \leq x \cdot \tan \frac{\pi}{3}$	$ y \leq (x + 1.5 \text{ cm}) \cdot \tan \frac{\pi}{6}$

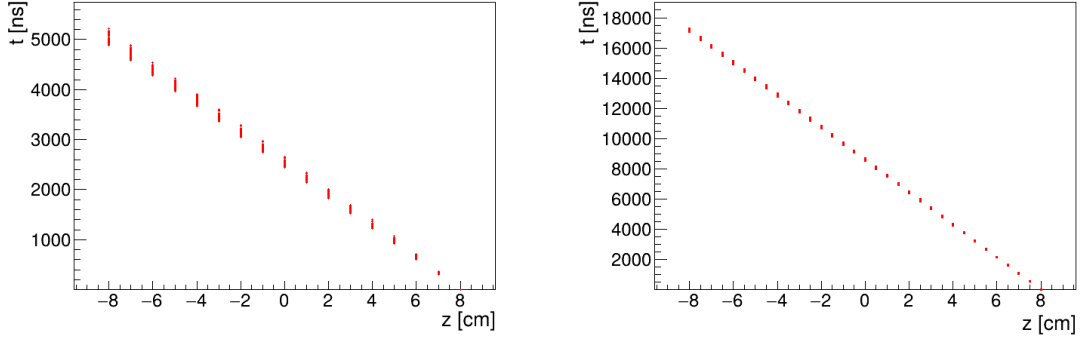


Figure 3.6: Dependence of the drift times of the simulated map $\bar{\mathcal{M}}$ on the z -coordinate. Two gas mixtures 90:10 (left) and 70:30 Ar:CO₂ (right) are compared. The spread is caused by varying Lorentz angles.

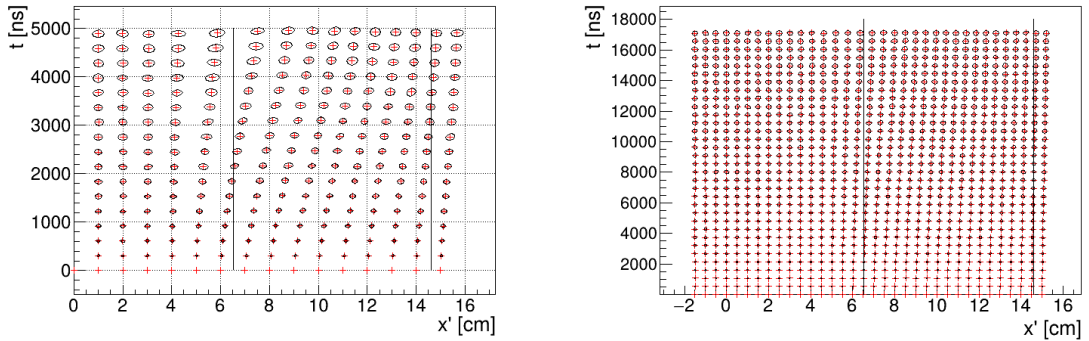


Figure 3.7: The $x't$ projection of the $\mathcal{M}(\mathbb{G}_{y=0})$ mapping of a part of the regular grid \mathbb{G} . The means $\bar{\mathcal{M}}(\mathbb{G}_{y=0})$ are marked with red crosses, and the diffusion error is denoted by black 95% confidence error ellipses computed from the diagonalized covariance matrices $\mathcal{M}_\Sigma(\mathbb{G}_{y=0})$. Two gas mixtures 90:10 (left) and 70:30 Ar:CO₂ (right) are compared. The first mixture shows differences of t for electrons with same initial z but different initial x . For the second mixture, these differences are negligible in comparison with the diffusion.

656 where \mathbf{X}_i represents the readout coordinates $(x'_i, y'_i, t_i)^T$ of the i -th electron. The
 657 matrix (resp. its submatrix) can then be used to plot error ellipsoid (resp. el-
 658 llipe). The axes correspond to the eigenvectors, errors along these axes for a given
 659 confidence level p can be computed using the chi-squared distribution

$$\sigma_i = \sqrt{\lambda_i \chi_k^2(p)}, \quad (3.9)$$

660 where λ_i is the corresponding eigenvalue and k is the number of degrees of free-
 661 dom.

662 As shown in Figs. 3.6 and 3.7, the drift times in the map are no longer propor-
 663 tional to the z -coordinate due to the varying Lorentz angles in the inhomogeneous
 664 magnetic field (see Equation 1.2). As expected, the effect is considerably larger in
 665 gases with higher drift velocities. Similarly, the drift distortion (i.e., its deviation
 666 from the vertical lines) is huge for the "faster" gas, but still significant for the
 667 "slower" one, as demonstrated in Figs. 3.8 to 3.10.

668 When evaluating the map inside the grid, we use trilinear interpolation (see
 669 Section 1.3.3). From now on, we will use the same symbol \mathcal{M} for this interpolated

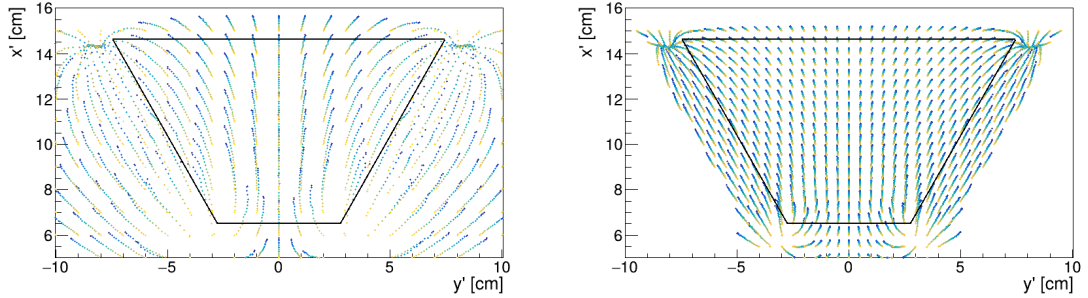
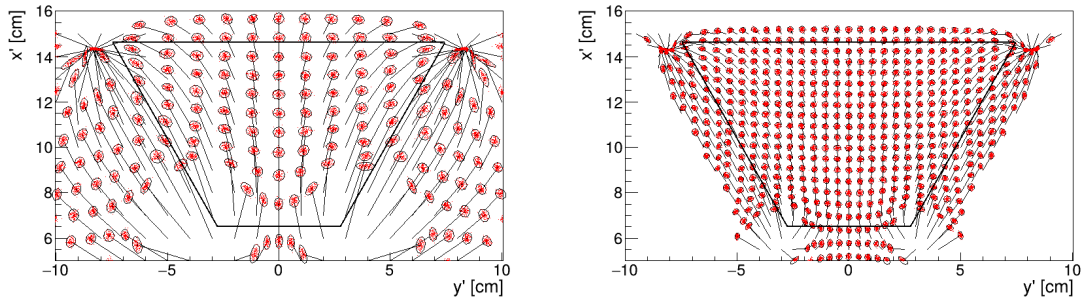
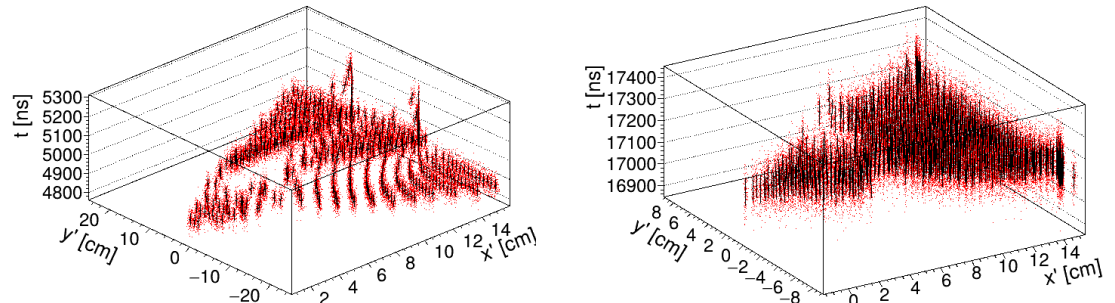


Figure 3.8: The regular grid \mathbb{G} projected by the mapping $\bar{\mathcal{M}}$ from the detector space onto the $x'y'$ plane (t is not plotted). Layers with lower z -coordinate (i.e., further away from the readout) are displayed with darker colors. The OFTPC volume is marked with black lines. Two gas mixtures 90:10 (left) and 70:30 Ar:CO₂ (right) are compared.



(a) The $x'y'$ projection of $\mathcal{M}(\mathbb{G}_8)$ (similar as in Figure 3.8), the diffusion is denoted with the 95% error ellipses from the diagonalized sample covariance matrices $\mathcal{M}_{\Sigma}(\mathbb{G}_8) \leftrightarrow$ Equation 3.8, and computed using Equation 3.9. The mean values $\bar{\mathcal{M}}(\mathbb{G}_8)$ are connected by black arrows with the corresponding starting position (x, y) of the simulated electrons. The OFTPC volume is marked with black lines.



(b) The full mapping $\mathcal{M}(\mathbb{G}_8)$, the diffusion is marked using standard error bars (black) from the diagonalized sample covariance matrices (Equations 3.8 and 3.9).

Figure 3.9: The $\mathcal{M}(\mathbb{G}_8)$ mapping of the bottom ($z = -8$ cm) layer \mathbb{G}_8 of the regular grid $\mathbb{G} \subset \mathcal{D}$. It includes both the mapping of means $\bar{\mathcal{M}}$ and of covariances \mathcal{M}_{Σ} . Individual electrons from the map simulation are marked with red dots. Two gas mixtures 90:10 (left) and 70:30 Ar:CO₂ (right) are compared.

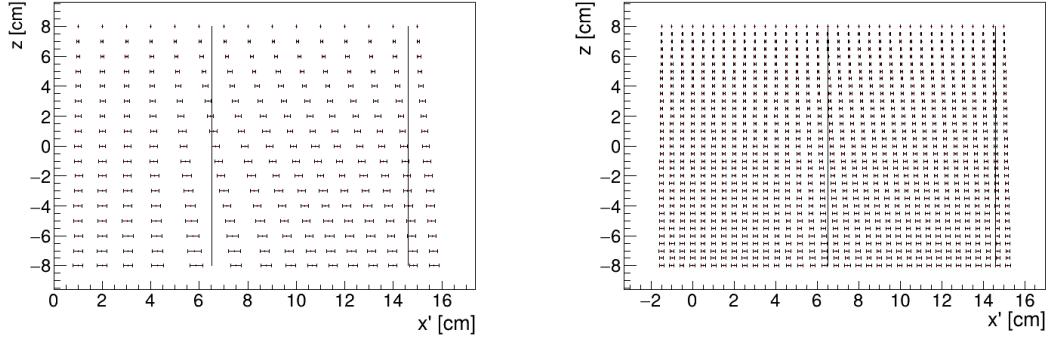


Figure 3.10: The readout coordinate x' for points on the grid $\mathbb{G}_{y=0}$ plotted against their initial coordinate z . The means are marked with red crosses, the diffusion in x' is denoted by standard error bars. Two gas mixtures 90:10 (left) and 70:30 Ar:CO₂ (right) are compared.

670 simulation.

671 Finally, we need to invert the map to get the original detector coordinates
 672 (x, y, z) from the given readout coordinates (x', y', t) . In our case, it is reasonable
 673 to assume that the mapping $\overline{\mathcal{M}}$ (we lose the information about the distribution
 674 (a wild idea how to recover this is in the Future section but it will only make sense
 675 if the GEM is already accounted for and is very preliminary as there are many
 676 factors to consider)) is one-to-one (as seen in the simulations). We implemented
 677 two methods for this purpose: the gradient descent search (Section 3.2.1) and
 678 interpolation on the inverse grid (Section 3.2.2).

679 The simulation (?) of the map is a computationally heavy task. For this rea-
 680 son, we use the MetaCentrum grid [3] to parallelize needed calculations. At first,
 681 this was done by evenly distributing the simulated electrons across the individual
 682 jobs in a simulation with only one electron per vertex in the regular grid \mathbb{G} with
 683 a spacing of one centimeter. Later, a more efficient approach was implemented,
 684 accounting for the varying lengths of the drift of individual electrons. If we index
 685 the vertices of \mathbb{G} in the order of increasing coordinates y, x, z (picture will make
 686 things clearer), we can express the number n_l of full XY layers (i.e., electrons with
 687 the same z coordinate, the mapping of one such layer is shown in Figure 3.9b)
 688 with index less than or equal to i

$$n_l(i) = \left\lfloor \frac{i}{n_{xy}} \right\rfloor, \quad (3.10)$$

689 where n_{xy} is the number of electrons in each XY layer calculated simply by count-
 690 ing the electrons that satisfy boundary conditions for x and y . These conditions
 691 should be mentioned above; sector condition + maximal x value. The number of
 692 electrons remaining in the top layer is then

$$n_r(i) = i \bmod n_{xy}. \quad (3.11)$$

693 Finally, we can calculate the sum of the drift gaps of electrons up to index i

$$d_{\text{sum}} = (z_{\max} - z_{\min})n_{xy}n_l - \frac{n_l(n_l - 1)}{2}n_{xy}l + n_r(z_{\max} - z_{\min} - n_l l). \quad (3.12)$$

694 We then use a binary search algorithm to find the maximum index i such that
 695 the value of this sum is less than the fraction $\frac{\text{job id}}{\max \text{ job id}}$ of the total sum. This way
 696 we obtain the minimal and the maximal index of electrons simulated in the given
 697 job. Picture of the simulating grid (1 layer). zmin zmax also

698 The obtained map is then stored in a custom class template *Field*, could
 699 expand on that. Maybe earlier, since the same template is used for the magnetic
 700 field.

701 Simulation inside of one sector (at first double angle). Extra space on the sen-
 702 sor. Using qsub (not sure if important). Add plots of distortion of the coordinates.
 703

704 Images to add (comparison of both simulations):

- 705 • Already have a simple 2D map visualization from the RD51 presentation,
 706 can use it or make something better
- 707 • z vs. t plot
- 708 • XY plane distortion for different z values; with arrows and error bars, for
 709 all z -layers with different colors
- 710 • XZ plane ($y = 0$) distortion in x (maybe not necessary?)
- 711 • XT plot ($y = 0$) showing (small) distortion in drift times
 712

713 More images:

- 714 • Residuals of the continuous readout reconstruction.

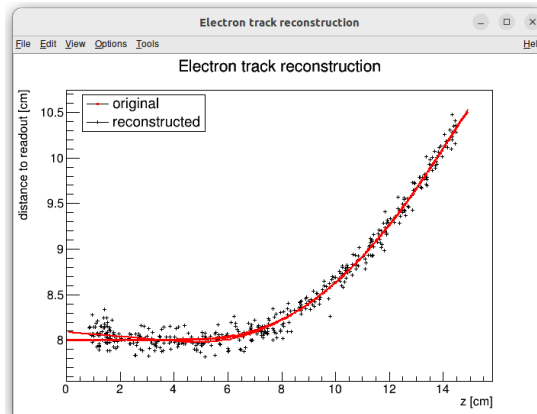


Figure 3.11: Example reconstruction with the map. Swap for better image, correct coordinates.

715 3.2.1 Gradient Descent Algorithm

716 The first implemented method of reconstruction uses a gradient descent algorithm
 717 to calculate an inversion of the map $\bar{\mathcal{M}}$ in a given point. Gradient descent is
 718 an iterative minimization algorithm for multivariate functions. Let $R \in \mathcal{R}$ be
 719 a point in the readout space; we want to find a point $D = (x, y, z) \in \mathcal{D}$ in
 720 the detector space such that

$$721 \quad \bar{\mathcal{M}}(D) = R = (x'_R, y'_R, t_R). \quad (3.13)$$

721 We define a function f_R in the readout space as a distance in this space:

$$f_R(x', y', t) = \sqrt{(x' - x'_R)^2 + (y' - y'_R)^2 + v_d^2(t - t_R)^2}, \quad (3.14)$$

722 where v_d is an approximation of the drift velocity in the TPC, obtained from
723 the reconstruction in Section 3.1 (there will be an image with the linear fit here).

724 We make an initial guess (actually in the original code we just take $z = 0$):

$$D_0 = (x'_R, y'_R, v_d t). \quad (3.15)$$

725 Assuming we have the n -th estimate D_n , we calculate the i -th component of
726 the gradient of $f_R \circ \bar{\mathcal{M}}$ numerically using central differences: (signs look correct)

$$[\nabla(f_R \circ \bar{\mathcal{M}})]^i(D_n) \approx \frac{f_R(\bar{\mathcal{M}}(D_n + s \cdot e^i)) - f_R(\bar{\mathcal{M}}(D_n - s \cdot e^i))}{2s}, \quad (3.16)$$

727 where $e^i \in \mathcal{D}$ is the i -th coordinate vector and s is the step size. The step size
728 should be sufficiently small; initially, we set it as a fraction $s = \frac{l}{10}$ of the map's
729 grid spacing l . During the minimization, we check that $f_R(\bar{\mathcal{M}}(D_n)) < 10s$ at all
730 times (s can (?) change – check). When using trilinear interpolation, it would be
731 more efficient to calculate the gradient explicitly (\pm same result). This could be
732 implemented inside the *Field* template class. The next iteration can be calculated
733 as follows:

$$D_{n+1} = D_n - \gamma \nabla(f_R \circ \bar{\mathcal{M}})(D_n), \quad (3.17)$$

734 where $\gamma \in \mathbb{R}^+$ is the damping coefficient. It should be set to a small enough
735 value to ensure convergence, but large enough for sufficient converging speed.
736 The minimization stops either when the error $f_R(\bar{\mathcal{M}}(D_n))$ drops below a specified
737 value or when the number of iterations exceeds a certain limit (in this case,
738 a message is printed into the console). The parameters of this method can be
739 further optimized (e.g., a better choice of γ , gradient computation); instead, we
740 later decided to use the interpolation on the inverse grid described in the next
741 section.

742 Measure reconstruction duration and compare it with the inverse grid inter-
743 polation? Also compare the result? Typical evolution of D_n during search. Not
744 sure if this has to be cited.

745 3.2.2 Interpolation on the Inverse Grid

746 Interpolation should be generally faster than the gradient descent since we don't
747 need to iterate. We also don't need to optimize it to improve performance, if
748 it's too slow we can even calculate the coefficients for the entire map before
749 reconstruction (again, do some profiling).

750 The best current algorithm uses the interpolation on the inverse grid. Rather
751 than inverting the trilinearly interpolated map using a numerical minimization
752 method as in the previous section, we take advantage of the fact that the map
753 $\bar{\mathcal{M}}$ is one-to-one (isomorphism is supposed to preserve structure, not sure how
754 to interpret that here, not the best description, we already (kind of) assume it
755 is a bijection by saying we will invert it). Since we have simulated values of this
756 map on a regular grid in the detector space \mathcal{D} , we also know the inverse map $\bar{\mathcal{M}}^{-1}$

757 on the irregular inverse grid in the readout space \mathcal{R} . To get an approximation
 758 of the inverse map in the entire readout space, we can use interpolation (**general**
 759 **concept, the specific choice is described below**).

760 Since the inverse grid is irregular, trilinear interpolation cannot be applied.
 761 Given that the simulated map is dense enough to provide a good approximation
 762 considering the size of our pads, we can adopt a similar approach.² As shown in
 763 Equation 1.21 in Section 1.3.3, trilinear interpolation (**shouldn't need an article**
 764 **when talking about a general concept**) can be expressed as a polynomial:

$$\hat{f}(x, y, z) = axyz + bxy + cxz + dyz + ex + fy + gz + h, \quad (3.18)$$

765 where a, b, c, d, e, f, g, h are coefficients uniquely determined by the values of
 766 the function at the vertices of the interpolation cell (**can be calculated in the**
 767 **way shown in the mentioned equation, not sure what more to add**). We can gen-
 768 eralize this for a function defined on an irregular grid. Given the function values
 769 at any eight points, we can write a system of eight linear equations

$$\begin{pmatrix} x_1y_1z_1 & x_1y_1 & x_1z_1 & y_1z_1 & x_1 & y_1 & z_1 & 1 \\ \vdots & \vdots \\ x_8y_8z_8 & x_8y_8 & x_8z_8 & y_8z_8 & x_8 & y_8 & z_8 & 1 \end{pmatrix} \begin{pmatrix} a \\ \vdots \\ h \end{pmatrix} = \begin{pmatrix} f(x_1, y_1, z_1) \\ \vdots \\ f(x_8, y_8, z_8) \end{pmatrix}, \quad (3.19)$$

770 which has a unique solution for the coefficients for most values of (x_n, y_n, z_n) and
 771 $f(x_n, y_n, z_n)$, where $n \in \{1, \dots, 8\}$.

772 This approach introduces a small complication: finding the correct pseudo-
 773 cell (i.e., the image of eight vertices forming a cubic cell in the regular grid) in
 774 the inverse grid. The eight irregularly spaced vertices of this pseudocell do not
 775 define a unique volume, so there are multiple possible ways to partition \mathcal{R} into
 776 pseudocells, with no obvious choice among them.

777 We are currently ignoring this problem and performing binary search along
 778 x, y, z (in this order). It shouldn't matter too much because the 70/30 map
 779 doesn't cause such a big distortion and was even accidentally extrapolated for all
 780 z different from the central plane.

²A more complicated and computationally heavy alternative would be natural neighbor interpolation or Kriging.

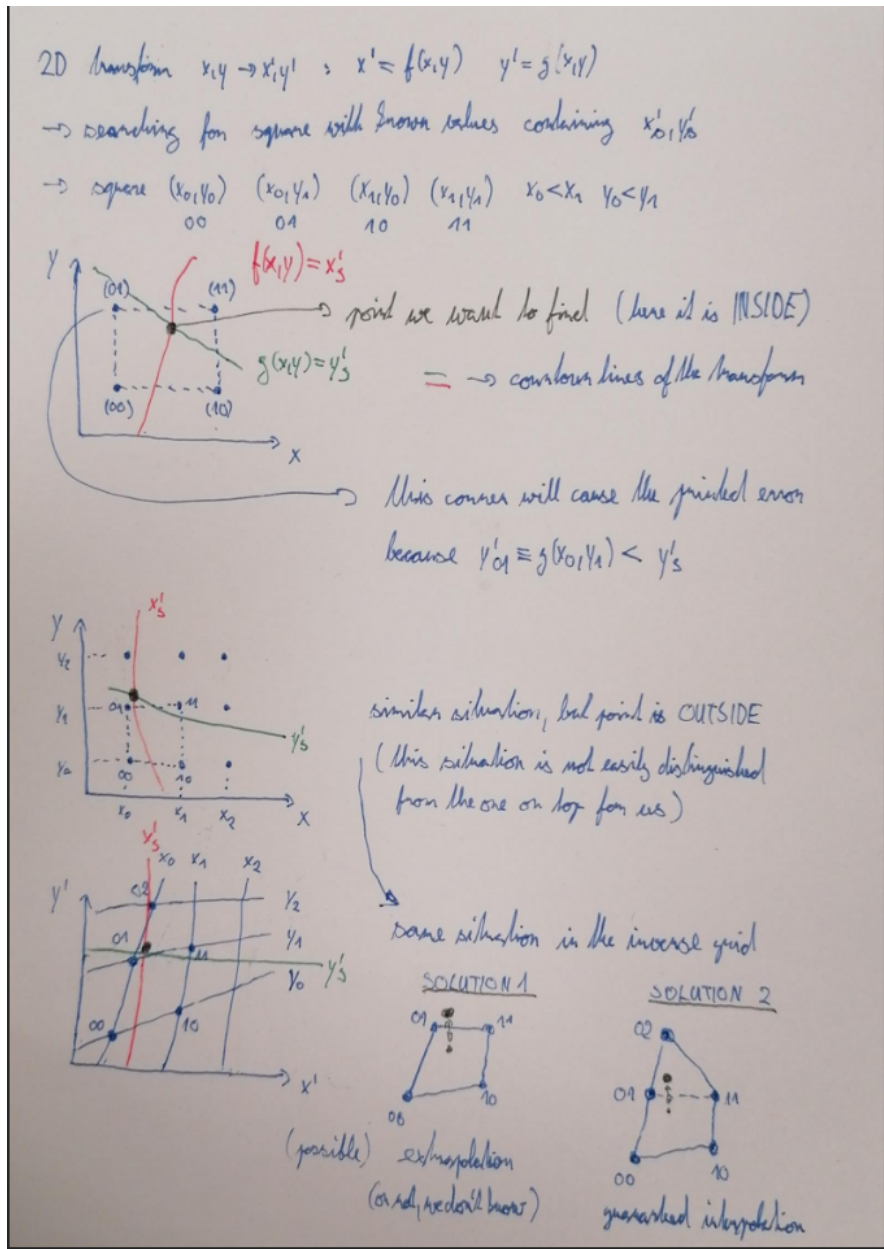


Figure 3.12: Selection of the points for interpolation. Create better images; use the explanation interpolation vs. extrapolation strange property. Solution 2 probably does not make much sense.

781 3.3 Discrete Reconstruction

782 Reconstruction with pads and time bins. Maybe testing different pads.

783 It is also possible to make this a subsection of the map, making the previous
784 subsections parts of a new subsection 'Map Inversion'.

In order to get a more realistic representation of a track measured in the OFTPC, we need to take the discretization of the position and time data into account. The readout of the OFTPC will consist of 128 pads, their layout is shown in Figure 1.6. Time is read out in discrete bins of size $t_{\text{bin}} = 100$ ns.

As the first approximation, we can neglect the multiplication in the triple-GEM.

790 and assume an ideal charge readout. The time measurement starts at the begin-
 791 ning of the electron/positron simulation (depending on the specific simulation it
 792 can correspond to the production in the target or when entering the OFTPC,
 793 here the specific time doesn't matter too much since the primary particle trav-
 794 els basically at light speed (30 ps/cm) which is circa immediate given the time
 795 binning). Randomize this time a bit and see what it does to the reconstruction.
 796 The readout coordinates $(x', y', t) \in \mathcal{R}$ of each ionization electron can be mapped
 797 to the pad coordinates $(n_{\text{pad}}, n_t) \in \mathcal{P}$:

$$n_{\text{pad}} = n: (x', y') \in \left[x_{1,n} - \frac{g}{2}, x_{2,n} + \frac{g}{2} \right] \times \left[y_{1,n} - \frac{g}{2}, y_{2,n} + \frac{g}{2} \right], \quad (3.20)$$

$$n_t = \left\lceil \frac{t}{t_{\text{bin}}} \right\rceil, \quad (3.21)$$

798 where $x, y_{1,n}$ and $x, y_{2,n}$ are the opposing pad corner coordinates, and g is the
 799 gap between the pads (described in detail in Section 1.3.2). This way, the clos-
 800 est pad is assigned to each readout position within the OFTPC volume³. Makes
 801 sense since the pads attract the electrons, the inhomogeneity of electric field is
 802 neglected. The number of electrons collected by each pad (i.e., collected charge)
 803 in each time bin is then counted and serves as a weight for the energy recon-
 804 struction. The reconstructed track consists of points for each $(n, n_t) \in \mathcal{P}$, we get
 805 these by reconstructing the position of a hypothetical electron with the readout
 806 coordinates of the pad/time bin center:⁴

$$\mathcal{D} \ni (x, y, z) = \overline{\mathcal{M}} \left(x_{c,n}, y_{c,n}, \left(n_t - \frac{1}{2} \right) t_{\text{bin}} \right). \quad (3.22)$$

³Some positions near the wall are not handled and some pads extend beyond the OFTPC volume. This is where an electric field simulation would come in handy.

⁴Mapping the center of the pad (along with the midpoint of the time bin) isn't necessarily the best approach since it might not correspond to the average parameters of an electron with these readout parameters.

807 4. Energy Reconstruction

808 The second stage is the reconstruction of the particle's energy using a fit of its
809 reconstructed track (see Section 3). We have tested three ways of reconstructing
810 the energy. Fitting is done using the MINUIT algorithm implemented in
811 ROOT [2]. Cite some CERN article directly on MINUIT, can add a section. Or
812 is it done using MIGRAD? The circle and RK4 probably was.

813 The **Cubic Spline Fit** was a tested and later rejected method of energy re-
814 construction. It uses smoothly connected piecewise cubic polynomials between
815 uniformly spaced nodes. The reconstructed energy is calculated using the fit pa-
816 rameters by computing the radius of curvature in different points of the fitted
817 curve using the known magnitude of the magnetic field perpendicular to the tra-
818 jectory. We rejected this method because the tuning of the fit turned out to be
819 unpractical compared to the other used methods. Reconstructs energy at every
820 position (even though the actual energy doesn't change much) and it might be
821 slower but no profiling has been done yet. Of course, it wasn't tested on the
822 newer track reconstruction methods at all.

823 The **Circle and Lines Fit** was chosen as an alternative since this corre-
824 sponds to the shape of a trajectory of a charged particle crossing a finite volume
825 with a homogeneous magnetic field. The energy of the particle can be estimated
826 using the fitted radius and the magnitude of the perpendicular magnetic field in
827 the middle of the TPC.

828 The **Runge-Kutta Fit** uses the 4th order Runge-Kutta numerical integration
829 described in Section 2.2. Initial parameters of the track (including the particle's
830 energy) are optimized so that the integrated trajectory fits to the reconstructed
831 one. This fit can also be performed as a single parameter (i.e., energy) fit if we
832 get the initial position and orientation of the particle on the entrance to the TPC
833 from previous detectors (TPX3 and MWPC, see Section 0.2).

834 4.1 Cubic Spline Fit

835 The first method for the estimation of the kinetic energy of the particle uses
836 a cubic spline fit. We use an electron track simulated using the microscopic

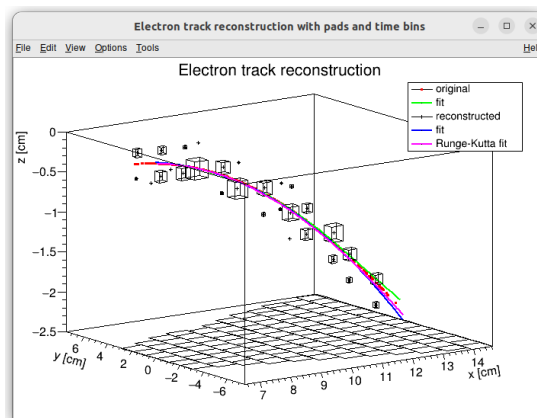


Figure 4.1: Example of a fitted reconstructed track. Swap for better image.

simulation, described in detail in Section 2.1.1. The track was reconstructed using the map described in Section 3.2.

In order to calculate the spline, we use the class *TSplines3* from ROOT. This allows us to evaluate the spline using the coordinates (x_n, z_n) of each node and the derivatives d_1, d_2 in the first and the last node. We can fit these parameters of a fixed amount of nodes to the simulated trajectory. We use the IMPROVE algorithm provided by the *TMinuit* class in ROOT (there are some guidelines for fonts in MFF UK template (Czech version) that I will eventually apply (see notes in the conclusion)). This algorithm attempts to find a better local minimum after converging (could reformulate a bit, taken word for word from some manual).

After the fit converges, we calculate an energy estimate using the radius of curvature, which we can extract from the fitted spline equation at every point of the trajectory. The part of the spline corresponding to a given node is defined as

$$z(x) = z_n + b\Delta x + c(\Delta x)^2 + d(\Delta x)^3, \quad (4.1)$$

where $\Delta x = x - x_n$ and b, c, d are coefficients. Using this equation, we derive the radius of curvature¹ as:

$$r(x) = \frac{(1 + z'^2(x))^{\frac{3}{2}}}{z''(x)} = \frac{(1 + (b + 2c\Delta x + 3d(\Delta x)^2)^2)^{\frac{3}{2}}}{2c + 6d\Delta x}. \quad (4.2)$$

Based on the geometry of our detector, we assume that the magnetic field satisfies $\mathbf{B}(x, 0, z) = (0, B(x, z), 0)$ for a track in the XZ plane. Since the electron is relativistic, the effect of the electric field on its trajectory is negligible. The Lorentz force F_L is then always perpendicular to the momentum of the electron and acts as a centripetal force F_c (not quite sure how to handle this then?):

$$\begin{aligned} \mathbf{F}_L &= \mathbf{F}_c, \\ \|e\mathbf{v} \times \mathbf{B}\| &= \frac{\gamma m_e v^2}{r}, \\ ec\beta B &= \frac{E_{0e}\beta^2}{r\sqrt{1 - \beta^2}}, \end{aligned} \quad (4.3)$$

$$\sqrt{1 - \beta^2} = \frac{E_{0e}\beta}{ecBr},$$

$$\beta^2(x) = \left[1 + \left(\frac{E_{0e}}{ecB(x, z(x))r(x)} \right)^2 \right]^{-1}, \quad (4.4)$$

where e is the elementary charge, c is the speed of light in vacuum, m_e is the rest mass of electron, $E_{0e} = m_e c^2$ is its rest energy, γ is the Lorentz factor, \mathbf{v} is the velocity of the electron, and $\beta = \frac{v}{c}$. The kinetic energy for a given point on the trajectory is then given as

$$E_{\text{kin}}(x) = \left(\frac{1}{\sqrt{1 - \beta^2(x)}} - 1 \right) E_{0e}. \quad (4.5)$$

¹For the general formula see https://en.wikipedia.org/wiki/Curvature#Graph_of_a_function.

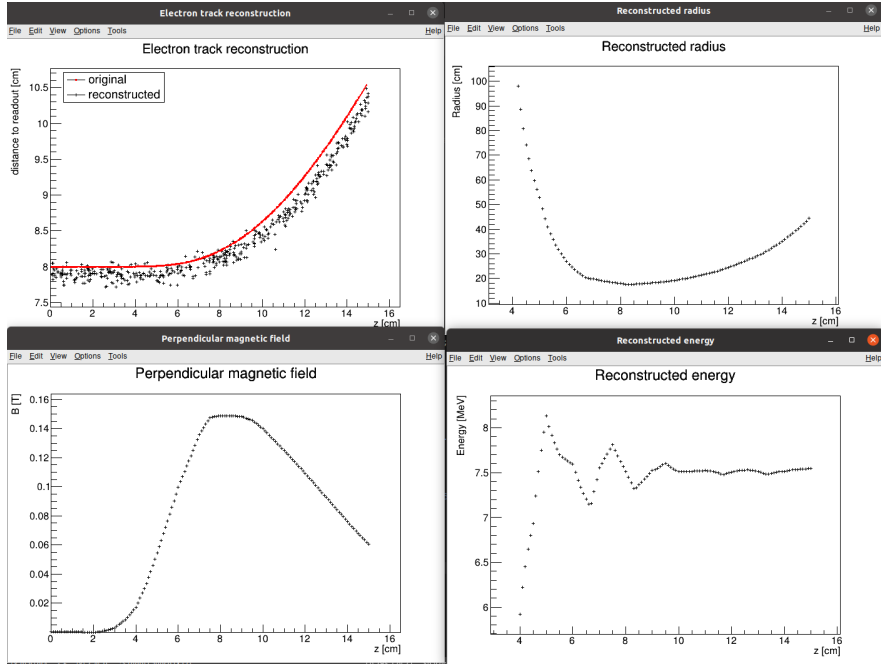


Figure 4.2: First attempt at a track reconstruction using only the drift velocity. Spline energy reconstruction attempt. Swap for better image(s) – subfigure environment, correct coordinates.

861 We can then average these estimates at multiple points (possibly using some
 862 weights to account for the change in accuracy, this wasn't optimized and we just
 863 ended with the graph) to get a single value. This method was later rejected in
 864 favor of the circle and lines fit (the name was already established at the beginning
 865 of the chapter) described in the next section. Add some figures.

866 4.2 Circle and Lines Fit

867 Another way to estimate the particle's kinetic energy is to fit its (??) trajectory
 868 with a circular arc with lines attached smoothly. This shape of trajectory cor-
 869 responds to a movement of a charged particle through a homogeneous magnetic
 870 field perpendicular to the particle's momentum and limited to a certain volume.
 871 In general, the shape of such a trajectory with a non-perpendicularly oriented
 872 momentum is a spiral. In our case, the magnetic field is approximately toroidal
 873 and the particle motion is nearly perpendicular to it (verify, could add some
 874 magnetic field plots in different vertical planes; shouldn't have a big effect on the
 875 reconstructed radius anyway). At first, we tested a 2D version of this fit, then
 876 we adapted it to 3D.

877 The field in our detector is not homogeneous, it is therefore not entirely clear
 878 what value of magnetic field should be used along with the fitted radius (using
 879 equations 4.4 and 4.5) to get the best estimate for the kinetic energy. Since we
 880 only use this method as the first iteration of the particle's energy that we later
 881 refine, an optimal solution of this problem is not required. Instead, we tested two
 882 options: taking the value of the field in the middle of the fitted circular arc (or
 883 is it in the middle x of the OFTPC?) and taking the average field along it. We

haven't really tried to plot this for multiple tracks, but these estimates are saved somewhere and could be plotted.

4.2.1 Two-dimensional fit

In the 2D case, the fitted function used for the electron track² described in Section 2.1.1 (one specific track at the time, technically this function doesn't work for a curvature that gets outside of the semicircle) is defined as follows:

$$z(x) = \begin{cases} a_1x + b_1 & x < x_1 \\ z_0 + \sqrt{r^2 - (x - x_0)^2} & x_1 \leq x \leq x_2 \\ a_2x + b_2 & x > x_2 \end{cases}, \quad (4.6)$$

where $a_{1,2}$ and $b_{1,2}$ are the parameters of the lines, (x_0, z_0) is the center of the circle, r is its radius, and $(x_{1,2}, z_{1,2})$ are the coordinates of the function's nodes. That means we have 9 parameters ($z_{1,2}$ are not used in the function) along with 2 continuity conditions and 2 smoothness conditions (9 parameters of the described function, 5 of them independent after taking the conditions into account). For the fit, we use the coordinates of the nodes and the radius of the circle, which gives us 5 independent parameters (only the radius has to be larger than half of the distance between nodes). The continuity conditions (combined with the relations for $z_{1,2}$) are

$$z_{1,2} = a_{1,2}x_{1,2} + b_{1,2} = z_0 - \sqrt{r^2 - (x_{1,2} - x_0)^2}, \quad (4.7)$$

the smoothness conditions are

$$a_{1,2} = \frac{x_0 - x_{1,2}}{\sqrt{r^2 - (x_{1,2} - x_0)^2}}. \quad (4.8)$$

Together with the Equation 4.7 we get the values of $b_{1,2}$

$$b_{1,2} = z_{1,2} - a_{1,2}x_{1,2}. \quad (4.9)$$

For the coordinates of the center of the circle, we can use the fact that the center has to lie on the axis of its chord. In other words, there is a value of a parameter t such that, using the parametric equation of the axis

$$\begin{pmatrix} x_0 \\ z_0 \end{pmatrix} = \begin{pmatrix} \frac{x_1+x_2}{2} \\ \frac{z_1+z_2}{2} \end{pmatrix} + t \begin{pmatrix} \frac{z_2-z_1}{2} \\ \frac{x_1-x_2}{2} \end{pmatrix}. \quad (4.10)$$

At the same time, the center has to be in a distance of r from the nodes:

$$\begin{aligned} (x_1 - x_0)^2 + (z_1 - z_0)^2 &= r^2, \\ \left(\frac{x_1 - x_2}{2} + \frac{z_1 - z_2}{2}t \right)^2 + \left(\frac{z_1 - z_2}{2} + \frac{x_2 - x_1}{2}t \right)^2 &= r^2, \\ \left(\left(\frac{x_2 - x_1}{2} \right)^2 + \left(\frac{z_2 - z_1}{2} \right)^2 \right)t^2 + \left(\frac{x_2 - x_1}{2} \right)^2 + \left(\frac{z_2 - z_1}{2} \right)^2 - r^2 &= 0. \end{aligned} \quad (4.11)$$

²Electron tracks bend towards negative z , we need to use the upper part of the circle

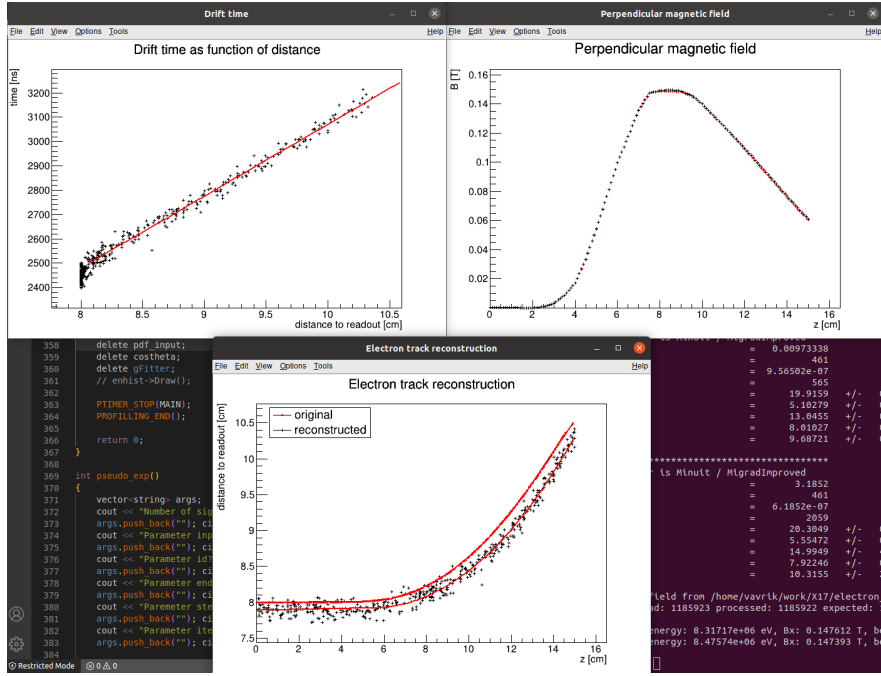


Figure 4.3: First attempt at a track reconstruction using only the drift velocity. Circle and Lines Fit in 2D. Swap for better image, correct coordinates. Bias should be described in the previous chapter, not here.

905 Since our electron track bends towards negative z and $x_2 > x_1$, we only care
906 about the solution with $t > 0$

$$t = \sqrt{\frac{r^2}{\left(\frac{x_2-x_1}{2}\right)^2 + \left(\frac{z_2-z_1}{2}\right)^2} - 1}, \quad (4.12)$$

$$x_0 = \frac{x_1 + x_2}{2} + \frac{z_2 - z_1}{2} \sqrt{\frac{r^2}{\left(\frac{x_2-x_1}{2}\right)^2 + \left(\frac{z_2-z_1}{2}\right)^2} - 1}, \quad (4.13)$$

$$z_0 = \frac{z_1 + z_2}{2} - \frac{x_2 - x_1}{2} \sqrt{\frac{r^2}{\left(\frac{x_2-x_1}{2}\right)^2 + \left(\frac{z_2-z_1}{2}\right)^2} - 1}.$$

907 The function defined in Equation 4.6 along with equations 4.8, 4.9, and 4.13
908 derived using the continuity and smoothness conditions (combined with the re-
909 lations for $z_{1,2}$) fully define our fitted function with parameters $r, x_{1,2}, z_{1,2}$. Some
910 pictures of the fit on the tested track. Results of the fit. Again, the actual fit
911 uses 8-z. Use GeoGebra schematics to generate a picture of 2D geometry.

912 4.2.2 Three-dimensional fit

913 Explain the geometry and least square method used for the 3D fit. Tested on
914 a Runge-Kutta sample, and with microscopic tracks + map simulation.

915 In three dimensions, the shape of a trajectory of a charged particle in a uniform
916 magnetic field is a cylindrical helix. Nevertheless, since we assume that the
917 field is approximately perpendicular to the particle's momentum at all times, we

will further approximate the trajectory with a circular arc (with lines attached smoothly).

We assume that the initial position $\mathbf{X}_0 = (x_0, y_0, z_0)$ and direction θ, φ (spherical angles as in Section 1.3.2) are known, since this information will be provided by TPX3 and MWPC layers. We could further refine it at the end of the current algorithm with some kind of global fit (all detector layers). The fit then has four free parameters (figure):

- the length of the first line l (as measured from the initial position),
- the radius of the circular arc r ,
- the central angle of the arc $\phi_{\max} \in [0, 2\pi]$,
- the direction of the curvature given by the angle $\alpha \in [0, 2\pi]$ (right-handed with respect to the particle direction, $\alpha = 0$ if the particle curves towards negative z in a plane given by $\hat{\mathbf{z}}$ and the direction vector).

Using these parameters, we can derive a parametrization of the whole curve. Let \mathbf{v} be the initial unit direction vector, i.e., using the spherical angles

$$\mathbf{v} = (\cos \varphi \cos \theta, \sin \varphi \cos \theta, \sin \theta)^T, \quad (4.14)$$

then we can parameterize the first line as follows:

$$\mathbf{X}_{L1}(t) = \mathbf{X}_0 + t\mathbf{v} \quad t \in [0, l]. \quad (4.15)$$

This gives us the starting point of the arc

$$\mathbf{X}_1 = \mathbf{X}_{L1}(l) = \mathbf{X}_0 + l\mathbf{v}. \quad (4.16)$$

The vector \mathbf{c}_1 that lies in the plane of curvature and points from \mathbf{X}_1 to the center of curvature can be calculated using a composition of rotations. First, we rotate \mathbf{v} to point in the $\hat{\mathbf{x}}$ direction, the normal for $\alpha = 0$ than points in the $-\hat{\mathbf{z}}$ direction, we apply the α rotation and reverse the rotations into the $\hat{\mathbf{x}}$ direction: (parameters are explained in the bullet points above)

$$\begin{aligned} \mathbf{c}_1 &= R_z(\varphi)R_y(-\theta)R_x(\alpha)R_y\left(\frac{\pi}{2}\right)R_y(\theta)R_z(-\varphi)\mathbf{v}, \\ &= R_z(\varphi)R_y(-\theta)R_x(\alpha)(-\hat{\mathbf{z}}), \\ &= \begin{pmatrix} \cos \varphi & -\sin \varphi & 0 \\ \sin \varphi & \cos \varphi & 0 \\ 0 & 0 & 1 \end{pmatrix} \begin{pmatrix} \cos \theta & 0 & -\sin \theta \\ 0 & 1 & 0 \\ \sin \theta & 0 & \cos \theta \end{pmatrix} \begin{pmatrix} 1 & 0 & 0 \\ 0 & \cos \alpha & -\sin \alpha \\ 0 & \sin \alpha & \cos \alpha \end{pmatrix} \begin{pmatrix} 0 \\ 0 \\ -1 \end{pmatrix}, \quad (4.17) \\ &= \begin{pmatrix} -\sin \alpha \sin \varphi + \cos \alpha \cos \varphi \sin \theta \\ \sin \alpha \cos \varphi + \cos \alpha \sin \varphi \sin \theta \\ -\cos \alpha \cos \theta \end{pmatrix}. \end{aligned}$$

Signs should be correct because right-handed rotation around y rotates z into x and this one is the opposite. Seems like in this part of the code θ is actually taken from the pole. Instead of the equator plane. Similarly by rotating $\hat{\mathbf{y}}$, we can get the normal vector $\mathbf{n} = \mathbf{v} \times \mathbf{c}_1$ perpendicular to the plane of the trajectory:

$$\mathbf{n} = R_z(\varphi)R_y(-\theta)R_x(\alpha)\hat{\mathbf{y}} = \begin{pmatrix} -\cos \alpha \sin \varphi - \sin \alpha \cos \varphi \sin \theta \\ \cos \alpha \cos \varphi - \sin \alpha \sin \varphi \sin \theta \\ \sin \alpha \cos \theta \end{pmatrix}. \quad (4.18)$$

944 This allows us to express the coordinates of the center \mathbf{C} of the circular arc:

$$\mathbf{C} = \mathbf{X}_1 + r\mathbf{c}_1. \quad (4.19)$$

945 We can then get the parametrization and the endpoint of the circular arc using
946 Rodrigues' rotation formula: (all parameters explained in the bullet points above)

$$\begin{aligned} \mathbf{c}_2 &= \mathbf{c}_1 \cos \phi_{\max} + (\mathbf{n} \times \mathbf{c}_1) \sin \phi_{\max} + \mathbf{n}(\mathbf{n} \cdot \mathbf{c}_1)(1 - \cos \phi_{\max}), \\ &= \mathbf{c}_1 \cos \phi_{\max} - \mathbf{v} \sin \phi_{\max}, \end{aligned} \quad (4.20)$$

$$\mathbf{X}_C(\phi) = \mathbf{C} - r(\mathbf{c}_1 \cos \phi - \mathbf{v} \sin \phi) \quad \phi \in [0, \phi_{\max}], \quad (4.21)$$

$$\mathbf{X}_2 = \mathbf{X}_C(\phi_{\max}) = \mathbf{C} - r\mathbf{c}_2, \quad (4.22)$$

947 and if we define the direction vector of the second line, we also get its parametriza-
948 tion

$$\mathbf{w} = \mathbf{v} \cos \phi_{\max} + (\mathbf{n} \times \mathbf{v}) \sin \phi_{\max} = \mathbf{v} \cos \phi_{\max} + \mathbf{c}_1 \sin \phi_{\max}, \quad (4.23)$$

$$\mathbf{X}_{L2}(s) = \mathbf{X}_2 + s\mathbf{w} \quad s \in [0, \infty). \quad (4.24)$$

949 The fit is performed as a (weighted) least square minimization (MIGRAD
950 ROOT), therefore we need to derive the distance of any point \mathbf{P} to the fitted
951 curve. For the first line, we simply compute the parameter value of the closest
952 point on the line:

$$\begin{aligned} t_P &= \mathbf{v} \cdot (\mathbf{P} - \mathbf{X}_1), \\ d_{P1} &= \|\mathbf{P} - \mathbf{X}_{L1}(t_P)\|. \end{aligned} \quad (4.25)$$

953 If the parameter value is outside of its bounds defined above, we take the bound-
954 ary value instead. The distance to the second line is computed likewise. For
955 the circular arc (specific circular arc in the fit), we find the closest point (on the
956 arc) by projecting the center connecting line onto the arc plane:

$$\mathbf{X}_{PC} = \mathbf{X}_C + r \frac{(\mathbf{P} - \mathbf{X}_C) - (\mathbf{n} \cdot (\mathbf{P} - \mathbf{X}_C))\mathbf{n}}{\|(\mathbf{P} - \mathbf{X}_C) - (\mathbf{n} \cdot (\mathbf{P} - \mathbf{X}_C))\mathbf{n}\|}, \quad (4.26)$$

$$d_{PC} = \|\mathbf{P} - \mathbf{X}_{PC}\| \quad (4.27)$$

957 Potential problem in the implementation – might not be correctly handling ϕ
958 out of bounds, the distance could be sometimes underestimated because of this.

959 The shortest distance out of d_{P1}, d_{PC}, d_{P2} is then taken as the distance to the curve. When
960 calculating energy with the average field, only the arc is considered. Middle field
961 in the current implementation taken in the middle x plane (intersection with
962 the curve). TVirtualFitter+MIGRAD, maximal num of iterations, toleration.
963 Different uncertainties in x, y, z not taken into account.

964 Fit details (parameter bounds, initial setting).

965 4.2.3 Testing on a Runge-Kutta sample

966 The three dimensional circle and lines fit was tested on a sample of Runge-Kutta
967 tracks with randomized parameters described in Section 2.2.1. These tracks of
968 primary electrons and positrons consist of points calculated with the RK4 algo-
969 rithm for a given proper time step (step can be adjusted by dividing by the gamma
970 factor → detector time). Fitting with circle only was also partially implemented
971 (didn't work but could be fixed/tuned).

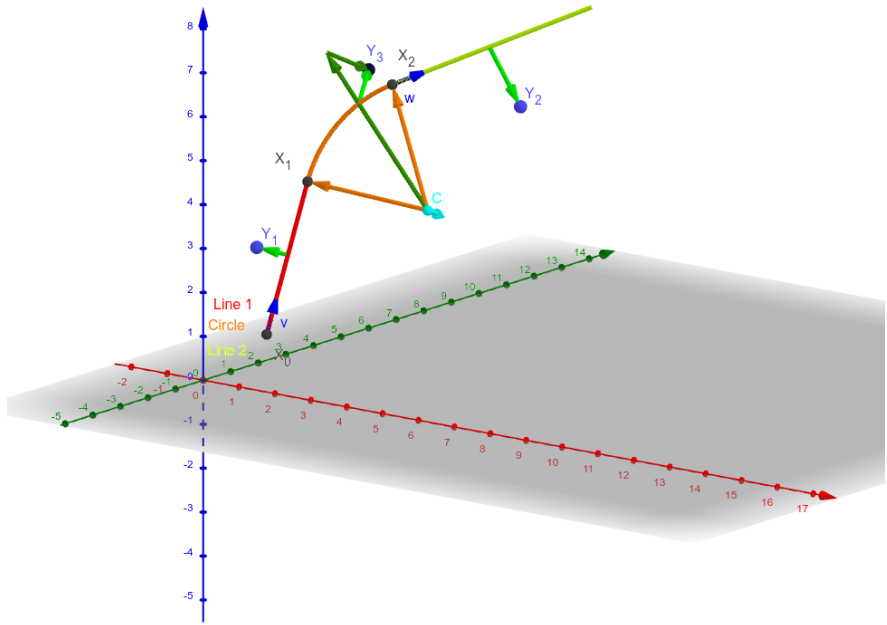


Figure 4.4: Circle and Lines Fit 3D geometry. Swap for better image.

972 4.3 Runge-Kutta Fit

973 The Runge-Kutta fit uses the Runge-Kutta 4th order (RK4) numerical integra-
 974 tion of the equation of motion (see Section 2.2) to find the best values of the track
 975 parameters – the track origin, initial velocity direction and the kinetic energy. In
 976 order to speed up the energy reconstruction, an initial guess of these parameters
 977 can be obtained from the 3D circle fit described in the previous section. Fur-
 978 thermore, assuming we know the track origin and orientation, we can perform
 979 a single parameter fit of the kinetic energy (**do some profiling and show that it is**
 980 **faster – below in the microscopic testing**).

981 The fit is performed as a least square minimization of the (weighted) distances
 982 of the track points (true ionization vertices from the simulation or reconstructed
 983 points). The simulated RK4 track consists of line segments with known endpoints,
 984 therefore we can calculate the distance of a point from this segment analogically
 985 to Equation 4.25 with \mathbf{v} given as a unit vector in the direction of the segment.

986 We need to find the segment with the lowest distance. We assume, that
 987 the distance $d_{\mathbf{P}}(\tau)$ of a point \mathbf{P} to the point on the track $\mathbf{X}(\tau)$ has a single
 988 minimum (local and global), no local maximum (except the interval endpoints)
 989 and no saddle point

$$\exists! \tau_{\min} \in [0, \tau_N]: (\forall \tau \in [0, \tau_N]: d_{\mathbf{P}}(\tau) \geq d_{\mathbf{P}}(\tau_{\min})) \vee \frac{dd_{\mathbf{P}}}{d\tau}(\tau_{\min}) = 0, \quad (4.28)$$

990 where N is the number of RK4 steps. This is a reasonable assumption for a track
 991 with an approximate shape of a circular arc with a radius r , since the distance d
 992 from a point \mathbf{C} on the corresponding circle of a point \mathbf{P} offset by a from the arc
 993 plane and by b from the arc's center when projected on its plane is given by the

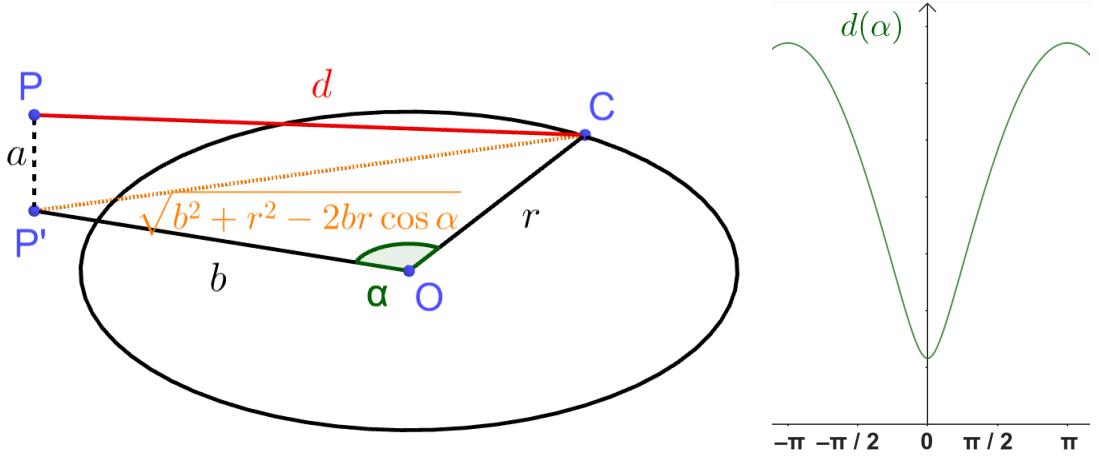


Figure 4.5: Demonstration of the convexity of the distance function $d(\alpha)$ for a circular track (see Equation 4.29).

994 law of cosines:

$$d^2 = a^2 + b^2 + r^2 - 2br \cos \alpha, \quad (4.29)$$

995 where α is the angle between points \mathbf{C} and \mathbf{P} as seen from the center of the circle
996 (see Figure 4.5). This function is strictly convex for $\alpha \in (-\frac{\pi}{2}, \frac{\pi}{2})$ and in our case,
997 the center of the arc lies outside of the detector and α is restricted to a small
998 interval around zero (especially considering that the initial guess should make the
999 fitted trajectory reasonably close to any relevant point, in the worst-case scenario,
1000 the distance is overestimated which should keep the fit from converging to such
1001 solutions).

1002 In a more general case, if we consider the vector $\mathbf{a}(\tau) = \mathbf{P} - \mathbf{X}(\tau)$ whose size
1003 is $\|\mathbf{a}(\tau)\| = d_{\mathbf{P}}(\tau)$, then we get

$$2d_{\mathbf{P}} \frac{dd_{\mathbf{P}}}{d\tau} = \frac{dd_{\mathbf{P}}^2}{d\tau} = \frac{d}{d\tau} \sum_i a_i^2 = 2 \sum_i a_i \frac{da_i}{d\tau} = 2\mathbf{a} \cdot \frac{d\mathbf{a}}{d\tau} = -2\mathbf{a} \cdot \frac{d\mathbf{X}}{d\tau}, \quad (4.30)$$

1004 therefore for the derivative of $d_{\mathbf{P}}(\tau)$ to be zero, $\mathbf{a}(\tau)$ has to be perpendicular
1005 to the tangent of the track. In 3D, for a given $\mathbf{X}(\tau)$, this condition restricts \mathbf{P}
1006 to a plane. This means that for a curving track we can find a point \mathbf{P} for any
1007 two points $\mathbf{X}(\tau), \mathbf{X}(\sigma)$ with non-parallel tangents that has $\frac{dd_{\mathbf{P}}}{d\tau}(\tau) = \frac{dd_{\mathbf{P}}}{d\tau}(\sigma) =$
1008 $= 0$, which violates the assumption 4.28. If we have a circle-and-lines track as
1009 described in the previous sections, such a point has to lie outside of the circular
1010 sector given by the arc.

1011 For a planar track, the envelope of all its normals is the evolute of the curve
1012 (i.e., the set of centers of all its osculating circles). If the track has a monotonous
1013 tangent angle

$$\alpha(\tau) = \text{atan} \frac{\frac{dX_2}{d\tau}}{\frac{dX_1}{d\tau}} \quad (4.31)$$

1014 with minimal and maximal α differing by less than π (i.e., the track changes
1015 direction by less than 180°), then all intersections of the track's normals must lie
1016 on the side of the evolute closer to the track (not obvious?, sometimes the sides
1017 are opposite?). At the same time, the intersection must lie in the half planes
1018 given by the normals at the beginning and the end of the curve and pointing

1019 away from the curve. Together, these three boundaries define a closed shape that
1020 will lie outside of the OFTPC for a typical track in our detector.

1021 With the assumption 4.28, we can find the segment on the RK4 track with
1022 the lowest distance to a given point \mathbf{P} using a binary search algorithm. Let
1023 the distance of the point from the n -th vertex be $d_{\mathbf{P},n}$. Then the difference
1024 $\Delta d_{\mathbf{P},n} = d_{\mathbf{P},n} - d_{\mathbf{P},n-1}$ satisfies

$$\begin{aligned}\Delta d_{\mathbf{P},n} &< 0 \quad \forall n \text{ such that } \tau_n < \tau_{\min}, \\ \Delta d_{\mathbf{P},n} &> 0 \quad \forall n \text{ such that } \tau_{n-1} > \tau_{\min}.\end{aligned}\tag{4.32}$$

1025 Therefore, we can search for the segment containing $d_{\mathbf{P},\min}$ with binary search
1026 starting with $\Delta d_{\mathbf{P},1}$ and $\Delta d_{\mathbf{P},N}$, then calculate the difference $\Delta d_{\mathbf{P},m}$ for the middle
1027 index $m = \left\lfloor \frac{N+1}{2} \right\rfloor$. If $\Delta d_{\mathbf{P},m} > 0$ (minor bug in the implementation – if the
1028 value for the maximal index is negative, it shouldn't change anything), we can
1029 replace the higher index with m , otherwise we replace the lower index. The search
1030 stops when the difference between the minimal and maximal index is one. Would
1031 it be better if they were the same (maybe not)? Then the minimal value is
1032 $d_{\mathbf{P},n-1}$ or $d_{\mathbf{P},N}$ and we can take the minimum of the distances from the two
1033 segments connected to $n-1$. Currently taking the maximal index (and starting
1034 at $N-2$ maximal index $\leftrightarrow N-1$ -th point), this should be equivalent, since either
1035 $\Delta d_{\mathbf{P},\max} > 0$ (in the code is equivalent to max-1 here) or we are at $N-1$. The
1036 minimum of the two distances still taken.

1037 Same details with MIGRAD etc. as previously.

1038 4.3.1 Testing on a microscopic sample

1039 The Runge-Kutta fit together with the 3D circle-and-lines pre-fit was tested
1040 on a sample of tracks simulated using the microscopic simulation described in
1041 Section 2.1. At first, few tracks with randomized initial parameters (same as
1042 the Runge-Kutta sample in Section 2.2.1) were generated for preliminary testing.
1043 Later, a sample with a grid-like distribution of track parameters was generated
1044 (see Section 2.1.2 for details).

1045 Initial parameters of the HEED track (also should be in the first testing track
1046 → subsection of microsim?). Initial parameters set in the circle fit (if electron set
1047 alpha one way, otherwise other way) and parameter bounds.

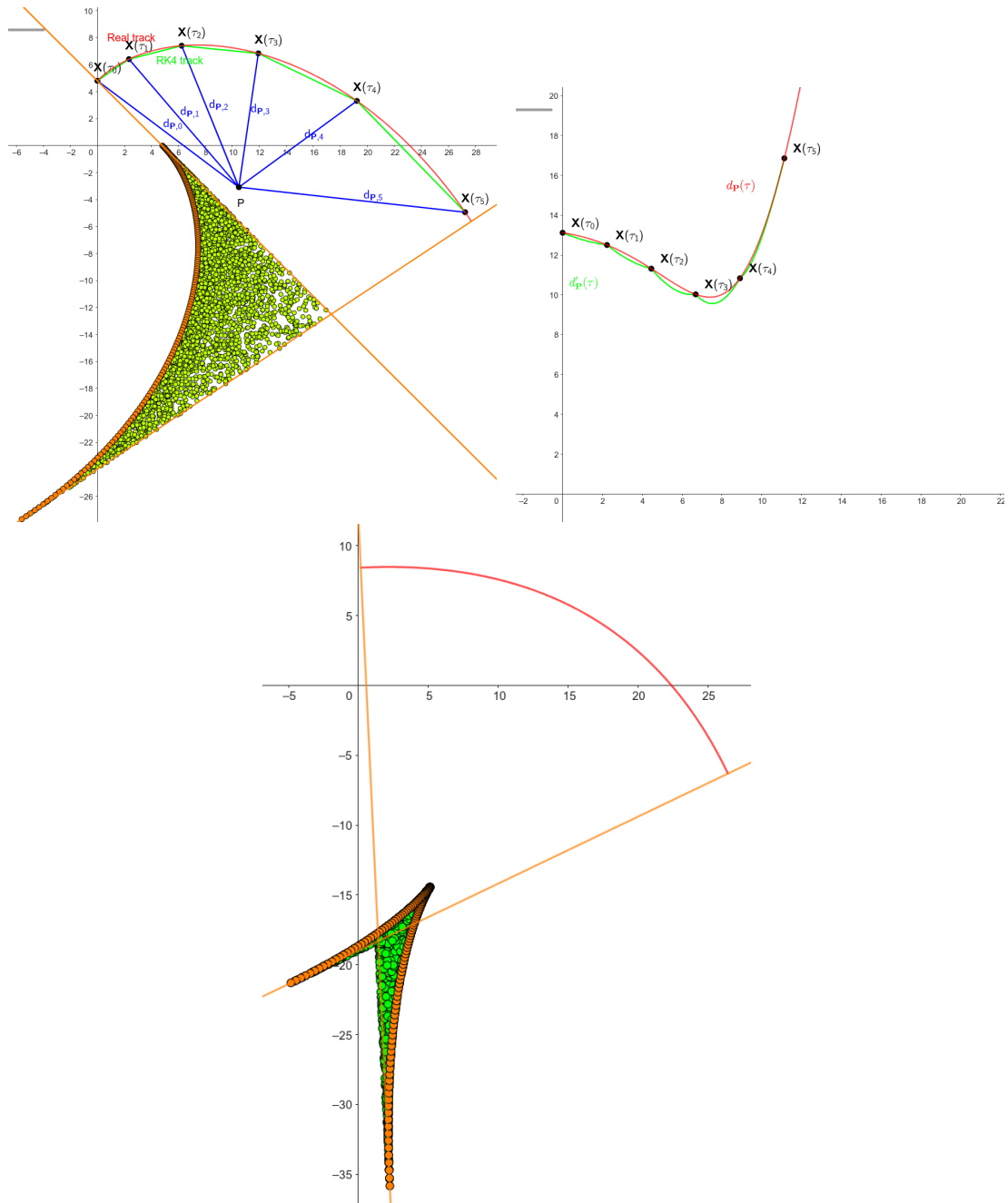


Figure 4.6: some provisional figures

Conclusion

1049 Here or at the end of each section. Something about the future of this work?

1050

1051 Notes

1052 General notes about the thesis:

- 1053 • Check that all of the classes and other code are marked the same way in
1054 the text. I used italics somewhere, could use different font for this instead.
- 1055 • Check unbreakable space in front of articles. Remove excessive article usage
1056 with proper nouns.
- 1057 • Currently using margins for single-sided printing (bigger on the left side).
- 1058 • Check that present tense is used
- 1059 • Active vs passive voice usage
- 1060 • American English quotation marks (") instead of British English (').
- 1061 • Some of the overfull hbox warnings might change if duplex printing is used
1062 (they generate black rectangles on the edge of the page), leaving them be
1063 for now
- 1064 • Check nobreakdash usage (is it always necessary)
- 1065 • Check capitalized references (e.g., Figure, Section, Equation)
- 1066 • Check $\backslash(...\backslash)$ math mode instead of $\$...$$. (actually unlike $\backslash[...\backslash]$ math mode,
1067 there is apparently no real benefit to this clumsy syntax)
- 1068 • Use siunitx package to ensure correct formatting, physics package for deriva-
1069 tives.
- 1070 • Check other stuff that's written in the MFF UK template. Apparently it
1071 has since been updated and there are some differences (check for them).
- 1072 • Check correct subscripts in equation (italics vs no italics)
- 1073 • Consistent bold marking of points/vectors
- 1074 • Correct footnotes (capital letters, etc.).
- 1075 • Might have to mention GeoGebra as per the non-commercial license agree-
1076 ment (Made with GeoGebra®) – maybe put it into acknowledgments next
1077 to the MetaCentrum credit? And list all of the figures where GeoGebra was
1078 used?
- 1079 • Maybe make some section outside of References specifically for literature?
1080 (such as the old CERN TPC review, ATOMKI review is currently not
1081 mentioned, not sure if some Wikipedia articles should get a mention or how
1082 do these things work)
- 1083 • Consistent use of `bm` vs `mathbf`

- Consistent use of $\bar{\mathcal{M}}$ instead of \mathcal{M} when talking about the map of the means (so most of the time)
 - Proper equation numbering when deriving a relation
 - Hugo should be mentioned somewhere in the title pages probably?
 - Consistent itemize/enumerate style (namely spacing) that looks good (ideally set by some macro? maybe the new MFF UK template will solve this?)
 - Consistent gas mixture notation (e.g., 90:10 Ar:CO₂). Maybe mention at the beginning that it is a molar ratio.
 - Labels of figures and tables – maybe in bold? Abbreviated?
 - Check graph labels, make them bigger if needed.
 - "The map" can be viewed as a mapping between spaces or just as a coordinate transform.
 - Maybe switch to cleverref.
 - siunitx qty not SI
- 1098 Random notes:
- Terminology consistency – ionization/primary/secondary electrons
 - Consistent TPC vs OFTPC acronym usage in the text or individual chapters.
 - Only electrons that start and end in the sector closer than 0.5 cm are used for reconstruction (newest version).
 - Attachment, Penning transfer and secondary ionization not considered in the microscopic simulation.
 - Suspicious artifacts of trilinear interpolation in Figure 1.7. **Fixed – integers instead of doubles in the implementation, influenced reconstruction SIGNIFICANTLY (but not simulation).**
 - Profiling of the reconstruction!!!! Find out what's taking the most time (probably Runge-Kutta integration which the fit calls a lot). Could gradually decrease the step size to refine the fit instead of making it small right away (arbitrarily small – the effect of this was never tested). This could take some time to do properly (find a profiler or make profiling macros).
 - Slow drift velocity good for z reconstruction, too low leads to recombination
 - Could add link to the GitHub repository, mention CMake? Details about simulating on MetaCentrum?
 - The first used track had 8 MeV momentum $p = \gamma mv$ (not kinetic energy $E_{\text{kin}} = (\gamma - 1)mc^2 = \sqrt{p^2c^2 + m^2c^4} - mc^2 \approx 7.5$ MeV)
 - Maybe cite Garfield++ user manual instead?
 - Using TRandom3 for random number generation.
 - Does the RK fit error correlate with the actual error?

- 1122 • Some Garfield settings in micro track generation probably not mentioned

1123 Future

1124 Things planned for the future:

- 1125 • Testing the reconstruction algorithm by measuring real particles with a known energy distribution.
- 1127 • The **Fast Simulation with Ionization Electron Map** is planned for the future. It will use the HEED program [31] to simulate the primary particle and the Ionization Electron Map (see Section 3.2) to simulate the drift of secondary electrons. It should be significantly faster than the Microscopic Simulation but offer comparable precision since it will rely on an already simulated drift map. (Primary track simulated in HEED. Readout parameters by interpolating the map. Diffusion from the map for randomization.)
- 1134 • Account for GEM, delta electrons, ...
- 1135 • Likelihood approach instead of least squares (if it improves the reconstruction significantly), we should at least use a better method than taking the center of the TPC bin.
- 1138 • More detailed electric field simulation (if needed, GEM will have more complex field, some irregularities in the field should be considered)
- 1140 • Account for the triggering in MWPC/TPX3 (particle travels from TPX3 to MWPC basically immediately – fraction of a nanosecond so there should be no significant difference)

1143

1144 Likelihood - inverse map

1145 If we wanted to further improve this procedure, taking into account the whole
 1146 map \mathcal{M} , we could make an "inverse map" from \mathcal{R} to distributions on \mathcal{D} . We could
 1147 achieve this by taking the normalized probability density of an electron with initial
 1148 coordinates (x, y, z) having readout coordinates (x', y', t) . If we fix (x', y', t) , we
 1149 get an unnormalized probability density $f(x, y, z) = \mathcal{M}_{(x,y,z)}(x', y', t)$ (assuming
 1150 that all initial coordinates are a priori equally likely). This could potentially
 1151 improve the discrete reconstruction if we take the mean value of this probability
 1152 density across the pad and time bin

$$f_{\text{pad, bin}}(x, y, z) = \frac{1}{A_{\text{pad}} \Delta t_{\text{bin}}} \int_{\text{pad, bin}} \mathcal{M}_{(x,y,z)}(x', y', t) dx' dy' dt \quad (4.33)$$

1153 and using it for a likelihood fit instead of using least squares. This still assumes
 1154 that all initial coordinates are equally likely which is clearly not the case for
 1155 a primary particle track. In the future, we could even use the fast track simulation
 1156 with the map (should be possible to make around 1000 tracks per minute per core
 1157 with current settings), create a big set of tracks with reasonable parameters and
 1158 use these to get an approximation of the probability distribution of the detector

1159 response. Some approximations would be necessary when interpreting the data to
1160 decrease the degrees of freedom of this distribution (we would have to pick a set of
1161 parameters and assume that some of them are independent). This could give us
1162 an idea about the best achievable resolution (how significantly will the detector
1163 response differ for a given change in energy). If the difference is significant, we
1164 could try to further improve the likelihood fit.

1165 Bibliography

- 1166 1. *Garfield++* [<https://garfieldpp.web.cern.ch/garfieldpp/>]. [N.d.].
1167 Accessed: 2023-05-18.
- 1168 2. BRUN, Rene; RADEMAKERS, Fons. Root — An Object Oriented Data Analysis Framework. *Nucl. Instrum. Methods Phys. Res. Sect. A: Accel. Spectrom. Detect. Assoc. Equip.* 1997, vol. 389, no. 1–2, pp. 81–86. Available from DOI:
1169 10.1016/s0168-9002(97)00048-x. Proceedings AIHENP'96 Workshop,
1170 Lausanne, Sep. 1996, See also <https://root.cern/>, Paper published in the
1171 Linux Journal, Issue 51, July 1998.
- 1172 3. *About MetaCentrum* [<https://metavo.metacentrum.cz/en/about/index.html>]. 2023. Accessed: 2024-11-27.
- 1173 4. ROSE, M. E. Internal Pair Formation. *Phys. Rev.* 1949, vol. 76, pp. 678–681.
1174 Available from DOI: 10.1103/PhysRev.76.678.
- 1175 5. ESSIG, R. et al. *Dark Sectors and New, Light, Weakly-Coupled Particles*.
1176 2013. Available from arXiv: 1311.0029 [hep-ph].
- 1177 6. DE BOER, F.W.N. et al. A deviation in internal pair conversion. *Phys. Lett. B*. 1996, vol. 388, no. 2, pp. 235–240. ISSN 0370-2693. Available from DOI:
1178 [https://doi.org/10.1016/S0370-2693\(96\)01311-1](https://doi.org/10.1016/S0370-2693(96)01311-1).
- 1179 7. BOER, F W N de et al. Excess in nuclear pairs near 9 MeV/ invariant mass. *J. Phys. G: Nucl. Part. Phys.* 1997, vol. 23, no. 11, p. L85. Available from DOI:
1180 10.1088/0954-3899/23/11/001.
- 1181 8. BOER, F W N de et al. Further search for a neutral boson with a mass around 9 MeV/c². *J. Phys. G: Nucl. Part. Phys.* 2001, vol. 27, no. 4, p. L29.
1182 Available from DOI: 10.1088/0954-3899/27/4/102.
- 1183 9. VITÉZ, Attila et al. Anomalous Internal Pair Creation in ⁸Be as a Signature
1184 of the Decay of a New Particle. *Acta Phys. Pol. B - ACTA PHYS POL B*.
1185 2008, vol. 39, p. 483.
- 1186 10. KRASZNAHORKAY, A. et al. Searching for a light neutral axial-vector boson
1187 in isoscalar nuclear transitions. *Frascati Phys. Ser.* 2012, vol. 56, p. 86.
- 1188 11. KRASZNAHORKAY, A. J. et al. Observation of Anomalous Internal Pair Creation in ⁸Be: A Possible Indication of a Light, Neutral Boson. *Phys. Rev. Lett.* 2016, vol. 116, no. 4. ISSN 1079-7114. Available from DOI: 10.1103/physrevlett.116.042501.
- 1189 12. TILLEY, D.R. et al. Energy levels of light nuclei A=8,9,10. *Nucl. Phys. A*. 2004, vol. 745, no. 3, pp. 155–362. ISSN 0375-9474. Available from DOI:
1190 <https://doi.org/10.1016/j.nuclphysa.2004.09.059>.
- 1191 13. SAS, N. J. et al. *Observation of the X17 anomaly in the ⁷Li(p,e⁺e⁻)⁸Be direct proton-capture reaction*. 2022. Available from arXiv: 2205.07744 [nucl-ex].
- 1192 14. KRASZNAHORKAY, A. J. et al. New anomaly observed in ⁴He supports the
1193 existence of the hypothetical X17 particle. *Phys. Rev. C*. 2021, vol. 104, no.
1194 4. ISSN 2469-9993. Available from DOI: 10.1103/physrevc.104.044003.

- 1207 15. TILLEY, D.R. et al. Energy levels of light nuclei A = 4. *Nucl. Phys. A*.
1208 1992, vol. 541, no. 1, pp. 1–104. ISSN 0375-9474. Available from DOI: [https://doi.org/10.1016/0375-9474\(92\)90635-W](https://doi.org/10.1016/0375-9474(92)90635-W).
- 1210 16. KRASZNAHORKAY, A. J. et al. New anomaly observed in ^{12}C supports the
1211 existence and the vector character of the hypothetical X17 boson. *Phys. Rev.*
1212 *C*. 2022, vol. 106, p. L061601. Available from DOI: 10.1103/PhysRevC.106.
1213 L061601.
- 1214 17. AJZENBERG-SELOVE, F. Energy levels of light nuclei A = 11,12. *Nucl. Phys.*
1215 *A*. 1990, vol. 506, no. 1, pp. 1–158. ISSN 0375-9474. Available from DOI:
1216 [https://doi.org/10.1016/0375-9474\(90\)90271-M](https://doi.org/10.1016/0375-9474(90)90271-M).
- 1217 18. KÁLMÁN, Péter; KESZTHELYI, Tamás. Anomalous internal pair creation.
1218 *The Eur. Phys. J. A*. 2020, vol. 56. Available from DOI: 10.1140/epja/
1219 s10050-020-00202-z.
- 1220 19. ALEKSEJEVS, A. et al. *A Standard Model Explanation for the "ATOMKI*
1221 *Anomaly*". 2021. Available from arXiv: 2102.01127 [hep-ph].
- 1222 20. FENG, Jonathan L. et al. Protophobic Fifth-Force Interpretation of the Ob-
1223 served Anomaly in ^8Be Nuclear Transitions. *Phys. Rev. Lett.* 2016, vol. 117,
1224 p. 071803. Available from DOI: 10.1103/PhysRevLett.117.071803.
- 1225 21. ANH, Tran The et al. Checking the 8Be Anomaly with a Two-Arm Electron
1226 Positron Pair Spectrometer. *Universe*. 2024, vol. 10, no. 4, p. 168. ISSN 2218-
1227 1997. Available from DOI: 10.3390/universe10040168.
- 1228 22. ABRAAMYAN, Kh. U. et al. *Observation of structures at ~ 17 and ~ 38*
1229 *MeV/c 2 in the $\gamma\gamma$ invariant mass spectra in pC, dC, and dCu collisions at*
1230 *p_{lab} of a few GeV/c per nucleon*. 2023. Available from arXiv: 2311.18632
1231 [hep-ex].
- 1232 23. THE MEG II COLLABORATION et al. *Search for the X17 particle in $^7\text{Li}(p, e^+e^-)^8\text{Be}$*
1233 *processes with the MEG II detector*. 2024. Available from arXiv: 2411.07994
1234 [nucl-ex].
- 1235 24. ABED ABUD, Adam et al. A Gaseous Argon-Based Near Detector to En-
1236 hance the Physics Capabilities of DUNE. 2022. Available from DOI: 10.
1237 48550/arXiv.2203.06281.
- 1238 25. LOKEN, Stewart C. et al. Performance of the Signal Processing System for
1239 the Time Projection Chamber. *IEEE Trans. on Nucl. Sci.* 1983, vol. 30, no.
1240 1, pp. 162–166. Available from DOI: 10.1109/TNS.1983.4332243.
- 1241 26. ADAMOVÁ, D. et al. The CERES/NA45 radial drift Time Projection Cham-
1242 ber. *Nucl. Instrum. Methods Phys. Res. Sect. A: Accel. Spectrom. Detect.*
1243 *Assoc. Equip.* 2008, vol. 593, no. 3, pp. 203–231. ISSN 0168-9002. Available
1244 from DOI: 10.1016/j.nima.2008.04.056.
- 1245 27. HILDÉN, T. et al. Optical quality assurance of GEM foils. *Nucl. Instrum.*
1246 *Methods Phys. Res. Sect. A: Accel. Spectrom. Detect. Assoc. Equip.* 2015,
1247 vol. 770, pp. 113–122. ISSN 0168-9002. Available from DOI: 10.1016/j.
1248 nima.2014.10.015.
- 1249 28. AHMED, Misbah Uddin. *Simulation of the electron and ion movement through*
1250 *a 4-GEM stack*. 2021. Institut für Kernphysik.

- 1251 29. MARMELAD. *3D interpolation2.svg*. 2025. Available also from: https://commons.wikimedia.org/wiki/File:3D_interpolation2.svg. Licensed
1252 under CC BY-SA 3.0 (<https://creativecommons.org/licenses/by-sa/3.0/legalcode>). Accessed: 9-April-2025.
- 1255 30. CMGLEE. *Trilinear interpolation visualisation*. 2025. Available also from:
1256 https://commons.wikimedia.org/wiki/File:Trilinear_interpolation_visualisation.svg. Licensed under CC BY-SA 3.0 (<https://creativecommons.org/licenses/by-sa/3.0/legalcode>). Accessed: 26-March-2025.
- 1259 31. SMIRNOV, I.B. Modeling of ionization produced by fast charged particles in
1260 gases. *Nucl. Instrum. Methods Phys. Res. Sect. A: Accel. Spectrom. Detect.*
1261 *Assoc. Equip.* 2005, vol. 554, no. 1, pp. 474–493. ISSN 0168-9002. Available
1262 from DOI: <https://doi.org/10.1016/j.nima.2005.08.064>.

1263 **Acknowledgments:** Computational resources were provided by the e-INFRA
1264 CZ project (ID:90254), supported by the Ministry of Education, Youth and Sports
1265 of the Czech Republic. **Figures that were drawn with GeoGebra. Maybe grant?**

1266 List of Figures

1267 0.1	The ATOMKI anomalous IPC measured for different nuclei.	5
1268 0.2	Results from the Hanoi spectrometer – angular e^+e^- pair correlations measured in the ${}^7\text{Li}(p, e^+e^-){}^8\text{Be}$ reaction at $E_p = 1225$ keV [21].	6
1269 0.3	Results from the MEG II experiments – angular correlation of e^+e^- pairs with $E_{\text{sum}} \in [16, 20]$ MeV measured in the ${}^7\text{Li}(p, e^+e^-){}^8\text{Be}$ reaction with proton beam energies 500 and 1080 keV. The 500 keV dataset is fitted with Monte Carlo of both the IPC deexcitation and the EPC produced by gammas [23].	7
1270 0.4	Schematics of the detector at the Van der Graaff facility at IEAP CTU.	7
1271 1.1	Particle identification in the PEP-4 TPC at SLAC based on the energy loss per distance $\frac{dE}{dx}$ [24].	9
1272 1.2	Schematic view of the PEP-4 TPC [25]. A charged particle produced in a collision in the beam pipe creates a spiral ionization track in the magnetic field. The central cathode then accelerates ionization electrons towards the endcap anode wires where they are multiplied and read out.	10
1273 1.3	A scanning electron microscope image of a GEM foil [27].	13
1274 1.4	Garfield simulation of an avalanche in a GEM hole [28]. An incoming electron (orange) is accelerated in the strong electric field of the GEM and causes further ionization multiplying the number of free electrons (orange). Most of the produced cations (red) are captured by the GEM cathode.	13
1275 1.5	Schematics of the first sector OFTPC with detector space coordinates.	16
1276 1.7	Magnetic field simulation results. The OFTPC volume and the vacuum tube are marked with black lines, the magnets are marked with red lines. The coordinates of the magnets from the CAD drawing seem to be 9/10 of the ones from the magnetic simulation (confirm and fix).	17
1277 1.6	Pad layout of the OFTPC and its parameters. Pads 102, 124 and 127 are irregular, the rest has the same dimensions.	17
1278 1.8	Visualization of trilinear interpolation as a composition of linear interpolations (inspired by [29]). We want to interpolate the value in the red point C. First we interpolate between the four pairs of blue points sharing the last two indices along the x -axis (Eq. 1.15), then between the two pairs of the resulting green points along the y -axis (Eq. 1.16) and finally between the two resulting orange points along the z -axis to get the final red value (Eq. 1.17).	18
1279 1.9	Geometric interpretation of trilinear interpolation as expressed in Equation 1.19. The colored dots represent the values in given points and the colored boxes represent the volume in the opposite corner by which the corresponding values are multiplied. The black dot represents the interpolated value which is multiplied by the entire volume [30].	19

1311	2.1 Comparison of drift lines for two different gas mixtures 90:10 and 1312 70:30 Ar:CO ₂ . The electron track is marked in black, the drift lines 1313 of the ionization electrons are marked in orange. In this example, 1314 we assume a larger OFTPC volume with readout at $z = 8$ cm.	22
1315	2.2 A visualization of a set of tracks from the grid-like testing sample 1316 with the same kinetic energy.	23
1317	2.3 A comparison of the HEED track from the microscopic simulation 1318 in Section 2.1.1 with a Runge-Kutta track with the same initial 1319 parameters and $\tau_{\text{step}} = 0.1$ ps (reducing the step further doesn't 1320 make a visible difference). In the view of the tracks on the left, 1321 the distance of the HEED ionization electrons from the RK4 track 1322 is exaggerated 1000 \times . On the right, the dependence of the HEED 1323 electrons residuals (i.e., their shortest distance to the RK4 track) 1324 on their z -coordinate is shown. The images look the same even 1325 for 100,000x smaller step, so the residuals are a result of some- 1326 thing that HEED does (maybe a different interpolation technique 1327 for the magnetic field? the pattern looks similar for two different 1328 tracks so it can't be scattering).	25
1329	3.1 Linear fit of the drift time t dependence on the distance to the 1330 readout $d_r = 8$ cm – z for the ionization electrons in 90:10 (left) 1331 and 70:30 (right) Ar:CO ₂ gas composition. Only electrons inside 1332 the TPC (red) are fitted. The parameters are $v_d = 3.39$ cm/ μ s, 1333 $d_0 = -0.41$ cm for 90:10, and $v_d = 0.939$ cm/ μ s, $d_0 = -0.11$ cm 1334 for 70:30 Ar:CO ₂	27
1335	3.2 Reconstruction (black) of the starting position of ionization elec- 1336 trons (red) using parameters obtained from the fit (Figure 3.1). 1337 Two gas compositions 90:10 (left) and 70:30 Ar:CO ₂ (right) are 1338 compared.	28
1339	3.3 Comparison of residuals (i.e., the distance from the reconstructed 1340 point to the simulated ionization electron starting point) depen- 1341 dence on x for two gas mixtures 90:10 (red) and 70:30 Ar:CO ₂ 1342 (blue).	28
1343	3.4 A 3D visualization of the mapping of means $\overline{\mathcal{M}}$ for the 90:10 1344 Ar:CO ₂ gas. A regular grid \mathbb{G} with $l = 1$ cm in the detector space 1345 is mapped to an irregular grid $\mathbb{G}^{-1} \equiv \overline{\mathcal{M}}(\mathbb{G})$ in the readout space.	29
1346	3.5 A test of the 90:10 Ar:CO ₂ map simulation with spacing $l = 1.5$ cm. 1347 The resulting drift lines of evenly spaced electrons are displayed in 1348 orange.	30
1349	3.6 Dependence of the drift times of the simulated map $\overline{\mathcal{M}}$ on the 1350 z -coordinate. Two gas mixtures 90:10 (left) and 70:30 Ar:CO ₂ 1351 (right) are compared. The spread is caused by varying Lorentz 1352 angles.	31

1353	3.7	The $x't$ projection of the $\mathcal{M}(\mathbb{G}_{y=0})$ mapping of a part of the regular grid \mathbb{G} . The means $\overline{\mathcal{M}}(\mathbb{G}_{y=0})$ are marked with red crosses, and the diffusion error is denoted by black 95% confidence error ellipses computed from the diagonalized covariance matrices $\mathcal{M}_\Sigma(\mathbb{G}_{y=0})$. Two gas mixtures 90:10 (left) and 70:30 Ar:CO ₂ (right) are compared. The first mixture shows differences of t for electrons with same initial z but different initial x . For the second mixture, these differences are negligible in comparison with the diffusion.	31
1361	3.8	The regular grid \mathbb{G} projected by the mapping $\overline{\mathcal{M}}$ from the detector space onto the $x'y'$ plane (t is not plotted). Layers with lower z -coordinate (i.e., further away from the readout) are displayed with darker colors. The OFTPC volume is marked with black lines. Two gas mixtures 90:10 (left) and 70:30 Ar:CO ₂ (right) are compared.	32
1367	3.9	The $\mathcal{M}(\mathbb{G}_{-8})$ mapping of the bottom ($z = -8$ cm) layer \mathbb{G}_{-8} of the regular grid $\mathbb{G} \subset \mathcal{D}$. It includes both the mapping of means $\overline{\mathcal{M}}$ and of covariances \mathcal{M}_Σ . Individual electrons from the map simulation are marked with red dots. Two gas mixtures 90:10 (left) and 70:30 Ar:CO ₂ (right) are compared.	32
1372	3.10	The readout coordinate x' for points on the grid $\mathbb{G}_{y=0}$ plotted against their initial coordinate z . The means are marked with red crosses, the diffusion in x' is denoted by standard error bars. Two gas mixtures 90:10 (left) and 70:30 Ar:CO ₂ (right) are compared.	33
1376	3.11	Example reconstruction with the map. Swap for better image, correct coordinates.	34
1378	3.12	Selection of the points for interpolation. Create better images; use the explanation interpolation vs. extrapolation strange property. Solution 2 probably does not make much sense.	37
1381	4.1	Example of a fitted reconstructed track. Swap for better image.	39
1382	4.2	First attempt at a track reconstruction using only the drift velocity. Spline energy reconstruction attempt. Swap for better image(s) – subfigure environment, correct coordinates.	41
1385	4.3	First attempt at a track reconstruction using only the drift velocity. Circle and Lines Fit in 2D. Swap for better image, correct coordinates. Bias should be described in the previous chapter, not here.	43
1389	4.4	Circle and Lines Fit 3D geometry. Swap for better image.	46
1390	4.5	Demonstration of the convexity of the distance function $d(\alpha)$ for a circular track (see Equation 4.29).	47
1391	4.6	some provisional figures	49

¹³⁹³ List of Tables

¹³⁹⁴	3.1 Comparison of parameters of two map simulations.	30
-----------------	--	----

¹³⁹⁵ List of Abbreviations

- ¹³⁹⁶ **GEM** Gas Electron Multiplier
- ¹³⁹⁷ **HEED** High Energy Electro-Dynamics
- ¹³⁹⁸ **IEAP CTU** Institute of Experimental and Applied Physics, Czech Technical
¹³⁹⁹ University in Prague
- ¹⁴⁰⁰ **IPC** Internal Pair Creation
- ¹⁴⁰¹ **EPC** External Pair Creation
- ¹⁴⁰² **Micromegas** MICRO-MEsh GAseous Structure
- ¹⁴⁰³ **MWPC** Multi-Wire Proportional Chamber
- ¹⁴⁰⁴ **OFTPC** Orthogonal Fields TPC
- ¹⁴⁰⁵ **RK4** Runge-Kutta 4th order
- ¹⁴⁰⁶ **TPC** Time Projection Chamber
- ¹⁴⁰⁷ **ToA** time-of-arrival
- ¹⁴⁰⁸ **ToT** time-over-threshold
- ¹⁴⁰⁹ **TPX3** Timepix 3